Ocean Engineering 368 (2026) 128497



Contents lists available at ScienceDirect

Ocean Engineering

journal homepage: www.elsevier.com/locate/oceaneng



Research paper

Numerical study on aerodynamic and wake characteristics of floating offshore wind turbines under partial wake conditions

Mingqiu Liu [a], Yao Zhong [b], Weiwen Zhao [a,*], Decheng Wan [a]

[a] Computational Marine Hydrodynamics Lab (CMHL), School of Ocean and Civil Engineering, Shanghai Jiao Tong University, Shanghai, 200240, China
[b] Powerchina Zhongnan Engineering Corporation Limited, Changsha, 410027, China

ARTICLE INFO

Keywords:
Floating offshore wind turbine
Partial wake
CFD
Wake characteristics

ABSTRACT

This study investigates the aerodynamic and wake characteristics of floating offshore wind turbines (FOWTs) under partial wake conditions using the fully coupled FOWT-UALM-SJTU solver. Atmospheric boundary layer inflow is generated via precursor simulations. Analysis of two turbines with varying lateral offsets reveals that while rotor-averaged inflow velocity increases with offset, inflow non-uniformity peaks under intermediate partial wake conditions. Consequently, the strongest unsteady aerodynamic responses occur when the rotor aligns with the transition region between the wake core and the free-stream. In this region, intensified wake meandering and non-uniformity lead to pronounced thrust and power fluctuations. Notably, the maximum normalized damage equivalent load is approximately 45% higher than that of the fully waked case. In terms of wake evolution, small offsets result in stronger wake superposition, deeper velocity deficits, higher turbulence-intensity peaks, and earlier blade-tip vortex breakdown, whereas large lateral offsets progressively weaken the upstream wake influence. At a 1*D* offset, the upstream turbine's direct influence significantly diminishes. These findings offer critical insights into wake assessment and layout design for floating wind farms.

1. Introduction

Wind energy has been extensively developed worldwide as a renewable energy source. Offshore wind energy offers several advantages, including no land occupation, abundant wind resources, and reduced noise pollution. As a result, an increasing number of countries have been actively expanding offshore wind power (Bhattacharya and Nikitas, 2025). Deep-water regions possess even richer wind resources, and with the advancement of floating offshore wind turbine (FOWT) technology, the exploitation of wind energy in these regions has become feasible. The FOWT platform is subjected to environmental loads and undergoes six degrees of freedom (6-DOF) motions, which directly influence its aerodynamic performance and wake characteristics. The resulting wake behavior further affects the power generation and structural loading of downstream turbines, making wake dynamics a key factor in determining the overall efficiency of wind farms (K. Wang et al., 2024). Therefore, investigating the aerodynamic and wake characteristics of FOWTs is of great importance for optimizing the operational efficiency of floating offshore wind farms.

Computational fluid dynamics (CFD) is a commonly used approach for investigating the aerodynamic and wake characteristics of FOWTs, as it allows controlled operating conditions and provides detailed flow-field information. To study the complex motion responses of FOWTs, many studies have simplified platform motions into prescribed 6-DOF components and their combinations. Previous research has shown that surge motion causes power fluctuations related to the surge period (Tran and Kim, 2016; Fang et al., 2021). Li et al. (2024) examined FOWT surge motion under laminar and turbulent inflow conditions and reported that periodic coherent structures induced by surge motion accelerated wake recovery. Cai et al. (2023) simulated FOWTs with prescribed pitch motion and found that pitch motion led to large variations in aerodynamic loads, thrust, and angle of attack. Under combined surge-pitch motion, FOWTs have been found to exhibit even stronger aerodynamic responses (Chen et al., 2021; Guo et al., 2022). Liu et al. (2025) analyzed the wake characteristics of FOWTs subjected to surge-pitch motion under atmospheric boundary layer (ABL) inflow and used dynamic mode decomposition (DMD) to reveal that platform motion excited a mode at the same frequency in the wake region, with stronger modal energy at lower motion frequencies. Li et al. (2022) investigated side-to-side motion and showed that, under low ambient turbulence,

* Corresponding author.
E-mail address: weiwen.zhao@sjtu.edu.cn (W. Zhao).

https://doi.org/10.1016/j.oceaneng.2026.128497
Received 27 April 2026; Received in revised form 15 September 2026; Accepted 27 September 2026
Available online 5 October 2026
0029-8018/© 2026 Elsevier Ltd. All rights are reserved, including those for text and data mining, AI training, and similar technologies.

wake meandering with larger amplitudes was triggered within a certain frequency range. Zhou et al. (2025) studied the influence of all six degrees of freedom on FOWT wakes and reported that, under laminar inflow, the wake length associated with heave, roll, and pitch motions was slightly shorter than that of fixed-bottom wind turbines (FBWTs), whereas the wake associated with sway, roll, and yaw became slightly longer.

Although prescribed six-degree-of-freedom motions provide fundamental understanding of the aerodynamic and wake behaviors of FOWTs, real FOWTs experience more complex motion responses driven by coupled wind-wave loads, leading to more complicated aerodynamic and wake variations. To capture these coupled responses, fully coupled simulations are necessary. Zhang and Kim (2018) employed a fully coupled approach to study a semisubmersible FOWT and reported that the thrust slightly increased while the power decreased compared with an onshore turbine. Yu et al. (2023) developed a hybrid aero-elastic-hydro-mooring model capable of capturing the interactions between FOWT motion and wake evolution. Cheng et al. (2019) developed the fully coupled solver FOWT-UALM-SJTU, which adopts the volume-of-fluid (VOF) method to simulate two-phase flow and the unsteady actuator line model (UALM) to capture turbine-flow interactions. The solver was validated for both aerodynamic and hydrodynamic responses of FOWTs. Huang and Wan (2019) applied the FOWT-UALM-SJTU solver to study a spar-type FOWT and showed that platform motion significantly altered the inflow structure and wake evolution. Xu et al. (2024) used the same solver to compare FOWT performance under uniform inflow, shear inflow, and ABL inflow, and found that atmospheric inflow caused stronger unsteadiness in power and thrust, faster wake recovery, and more pronounced wake meandering. These studies demonstrate that fully coupled aero-hydrodynamic interactions under combined wind-wave loading play a crucial role in shaping FOWT aerodynamics and wake dynamics.

In addition to the aerodynamic and wake variations induced by their own coupled responses under combined wind-wave loading, downstream FOWTs may also experience more complex responses due to the wakes of upstream turbines. Rezaeiha and Micallef (2021) investigated two FOWTs arranged in series and reported that, when the upstream turbine performed surge motion and the downstream turbine was fixed, the surge motion enhanced flow mixing in the wake, thereby accelerating wake recovery at the downstream rotor. Arabgolarcheh et al. (2023b, 2023a) studied two tandem FOWTs undergoing surge and pitch motions and found that the platform motions of the upstream turbine intensified the inflow non-uniformity at the downstream turbine; moreover, different phase lags between platform motions significantly modulated the power output and structural loads of the downstream turbine. Huang et al. (2023) employed the FOWT-UALM-SJTU solver to simulate two spar-type FOWTs arranged in series and showed that platform motion strengthened wake asymmetry, accelerated wake recovery, and strongly affected the performance of the downstream turbine. Li et al. (2025) analyzed three semi-submersible FOWTs and reported that, in a linear layout, the fluctuation amplitude of the downstream FOWT could be up to 25% higher than that of an FBWT, while in a staggered layout it could reach 80%. High-fidelity CFD approaches are capable of resolving detailed flow structures with high accuracy but require substantial computational resources. As a result, many studies have adopted medium-fidelity methods to investigate multi-turbine wake interactions. Wise and Bachynski (2020) used the FAST.Farm solver, which incorporates a dynamic wake model (DWM) to generate wake fields, and simulated two FOWTs in a tandem layout. Their results showed that platform motion amplified low-frequency wake oscillations and affected downstream turbine performance. Xue et al. (2022) used FAST.Farm to study two FOWTs in series and found that platform motion intensified wake-added turbulence and increased the unsteady aerodynamic loads of the downstream turbine. L. Wang et al. (2024) applied an aero-hydro-servo-elastic method together with the DWM to simulate two FBWTs and two FOWTs, and reported that platform motion accelerated wake recovery and reduced its impact on the downstream turbine. Xu et al. (2025) also used FAST.Farm to analyze two tandem FOWTs and showed that the downstream turbine subjected to upstream wake effects experienced substantially increased surge motion and structural loads compared with the unwaked condition. These studies indicate that wake interactions between FOWTs can exert complex effects on the aerodynamic responses and wake characteristics of downstream turbines.

Most existing studies on multiple FOWTs have focused on turbines arranged in a tandem layout. However, wind farm layout optimization and active yaw control strategies, which are adopted to improve wind farm efficiency, may result in downstream turbines that are not aligned with upstream ones, thereby exposing them to partial wake conditions. Partial wake refers to conditions where only a portion of the upstream wake overlaps the downstream rotor. Fleming et al. (2015) simulated two wind turbines and showed that yaw misalignment and staggered layouts produced partial wake situations, which significantly affected the downstream turbine's power output and structural loads. Lin and Porté-Agel (2022) reported that yaw-induced wake deflection generated highly asymmetric partial wake conditions for downstream turbines, leading to substantial changes in mean velocity deficit, turbulence intensity, and power distribution. Gao et al. (2024) found that the standard deviation of structural loads under partial wake conditions increased by 51% compared with full-wake conditions. Campaña-Alonso et al. (2024) examined two turbines placed at different lateral offsets and demonstrated that partial wake inflow induced large oscillations in the power coefficient and increased blade-root loads by 20%-30%. These studies have confirmed that partial wake conditions significantly affect the power output and structural loading of downstream turbines. However, most existing investigations have focused on FBWTs, while the platform motions of FOWTs may introduce additional complexity. Inflow conditions also represent a key factor influencing the aerodynamic and wake characteristics of FOWTs. Although many previous studies have used uniform inflow, real offshore conditions are increasingly dominated by atmospheric turbulence as turbine size increases, which strongly affects aerodynamic performance and wake behavior (Porté-Agel et al., 2020). Li et al. (2018) studied the influence of atmospheric inflow on the aerodynamic performance of FOWTs and found that power output was highly sensitive to atmospheric turbulence. Xu et al. (2023) reported that the power variation of semi-submersible FOWTs was mainly driven by inflow atmospheric turbulence, while the effect of platform motion was comparatively weaker. Zhou et al. (2022) examined the influence of inflow conditions on FOWT wake characteristics and observed faster wake spreading under atmospheric turbulence than under uniform inflow. These findings suggest that both the partial wake effect and ABL inflow are critical yet insufficiently explored factors for FOWTs.

In summary, although previous studies have extensively investigated FOWTs from the perspectives of platform motions, wake interactions, and ABL inflow effects, the aerodynamic responses and wake evolution of FOWTs under partial wake conditions with ABL inflow remain insufficiently understood. Existing multi-turbine studies mainly focus on fully waked conditions or specific turbine arrangements, whereas partial wake induced by lateral turbine offsets can lead to pronounced spatially non-uniform inflow across the rotor disk, and its effects on platform motions, instantaneous aerodynamic loads, and fatigue responses have not yet been fully clarified. Meanwhile, under partial wake conditions, how the non-uniformity of the upstream wake is further transmitted to the downstream turbine wake and affects its velocity deficit, turbulence distribution, and vortex structure evolution also remains to be investigated. To address these gaps, this study employs the validated FOWT-UALM-SJTU solver to investigate the interaction between two fully coupled FOWTs under ABL inflow with different lateral offsets of the downstream turbine. The ABL inflow is generated through precursor simulations. Starting from the rotor-disk inflow characteristics of the downstream turbine, its platform motions, thrust and power responses,

local blade aerodynamic states, and fatigue loads are further analyzed, while the downstream wake evolution is systematically examined in terms of velocity deficit, turbulence intensity, and vortex structures. The objective is to clarify how partial wake affects the mean performance and unsteady responses of FOWTs under ABL inflow conditions, and to provide a reference for turbine layout design and wake-effect assessment in floating wind farms.

This paper is organized as follows. Section 2 describes the numerical methodology. Section 3 presents the simulation setup and the mesh convergence analysis. Section 4 provides the results, including analyses of inflow characteristics, motion responses, aerodynamic characteristics, and wake characteristics. Finally, Section 5 summarizes the findings and offers the main conclusions.

2. Numerical methods

The numerical simulations in this study are conducted using the fully coupled FOWT-UALM-SJTU framework, which couples the in-house two-phase flow solver naoe-FOAM-SJTU with the unsteady actuator line model (UALM). The naoe-FOAM-SJTU solver is developed based on OpenFOAM and has been systematically validated under various operating conditions (Cao et al., 2013; Shen and Wan, 2014; Zhao and Wan, 2015; Cao and Wan, 2014; Wang et al., 2019), while the coupled FOWT-UALM-SJTU framework has been established and validated for FOWT simulations in previous studies (Cheng et al., 2019; Huang and Wan, 2019; Xu et al., 2024).

2.1. Governing equations

The fully coupled FOWT system is simulated using the three-dimensional Navier-Stokes equations, with the fluid assumed to be viscous and incompressible. The continuity equation and the momentum equations are expressed as follows:

$$\nabla \cdot \mathbf{U} = 0 \tag{1}$$

$$\frac{\partial(\rho \mathbf{U})}{\partial t} + \nabla \cdot (\rho \mathbf{U}\mathbf{U}) = -\nabla p_d - \mathbf{g} \cdot \mathbf{x} \nabla \rho + \nabla \cdot \left(\mu_{eff} \nabla \mathbf{U}\right) + \mathbf{f}_\sigma + \mathbf{f}_s + \mathbf{f}_\varepsilon \tag{2}$$

where, $\mathbf{U}$ represents the fluid velocity; ρ is the fluid density; p_d denotes the dynamic pressure, which is defined as the total pressure minus the static pressure; $\mathbf{g}$ is the gravity acceleration; $\mathbf{x}$ represents the Cartesian coordinate vector; μ_{eff} is the effective viscosity, which is defined as the sum of the molecular viscosity and the eddy viscosity; $\mathbf{f}_\sigma$ represents the source term associated with tension force of free surface; $\mathbf{f}_s$ denotes the wave absorption source term; $\mathbf{f}_\varepsilon$ is the body force source term induced by turbine aerodynamic loads, which is computed using the UALM. To accurately resolve the wake characteristics of FOWTs, the large eddy simulation (LES) is employed in this study.

2.2. Aerodynamic modeling

The actuator line model (ALM) is a commonly used approach for wind turbine aerodynamic modeling (Sørensen and Shen, 2002). The basic concept of ALM is to discretize each blade into a series of actuator points. The aerodynamic forces at these points are calculated based on blade element momentum theory and are applied to the flow field as body force source terms to represent the influence of the turbine on the surrounding flow. This approach avoids the high grid resolution required for blade resolved simulations and thus reduces the computational cost (Troldborg et al., 2007). Consequently, ALM is widely used in wind turbine wake studies (Churchfield et al., 2012; Porté-Agel et al., 2020).

In this study, the UALM is employed to model FOWTs. Compared with the conventional ALM, the UALM accounts for the additional velocity induced by platform motion when computing the relative wind speed (Cheng et al., 2019). Fig. 1 shows the velocity vectors of the blade element. The relative wind speed $\mathbf{U}_{rel}$ is defined as:

$$\mathbf{U}_{rel} = \mathbf{U}_\theta - \Omega r + \mathbf{U}_Z + \mathbf{U}_M \tag{3}$$

where, $\mathbf{U}_\theta$ and $\mathbf{U}_Z$ represent the tangential and axial components of inflow wind speed, respectively; Ω is the rotor speed; r denotes the length from the blade element to rotor center; $\mathbf{U}_M$ is the additional velocity induced by platform motion.

The local attack angle α is given by:

$$\alpha = \varphi - \beta, \varphi = \tan^{-1}\left(\frac{\mathbf{U}_Z + \mathbf{U}_{M,Z}}{\Omega r + \mathbf{U}_{M,\theta} - \mathbf{U}_\theta}\right) \tag{4}$$

where, φ denotes the local inflow angle; β is the local pitch angle. Based on the computed local attack angle and the airfoil data, the lift coefficient C_L and drag coefficient C_D are obtained. The body force is then computed as follows:

$$\mathbf{f} = (\mathbf{L}, \mathbf{D}) = \frac{1}{2}\rho |U_{rel}|^2 c(C_L \mathbf{e}_L + C_D \mathbf{e}_D) \tag{5}$$

where, L and D represent the lift and drag forces, respectively; c denotes the chord length; $\mathbf{e}_L$ and $\mathbf{e}_D$ are the unit vectors of lift and drag forces, respectively. By further integrating along the blade radial direction, the overall aerodynamic loads are obtained. It should be noted that, when projecting the aerodynamic loads onto the flow field, a distributed projection rather than a single-point application is required in order to avoid numerical singularities. In practice, a Gaussian kernel function is adopted in this study to smooth the aerodynamic loads at the actuator points. More details can be found in Cheng et al. (2019).

2.3. Hydrodynamic modeling

Within the FOWT-UALM-SJTU framework, the hydrodynamic module includes numerical wave generation and absorption, 6-DOF motion solving, and mooring system modeling. The solver is based on the finite volume method to discretize and solve the incompressible Navier-Stokes equations. The motion of floating structures is handled using a dynamic mesh technique (Cheng et al., 2019). The free surface of the two-phase flow is captured using the volume of fluid (VOF) method, and the corresponding transport equation is given as follows:

$$\frac{\partial \alpha_v}{\partial t} + \nabla \cdot \left[(\mathbf{U} - \mathbf{U}_g)\alpha_v\right] + \nabla[\mathbf{U}_r(1-\alpha_v)\alpha_v] = 0 \tag{6}$$

where, $\mathbf{U}_g$ denotes the velocity of grid nodes; $\mathbf{U}_r$ represents the velocity field used to compress the interface; α_v is the volume fraction. Values of $\alpha_v = 0$ and $\alpha_v = 1$ indicate that the computational cell is occupied by air

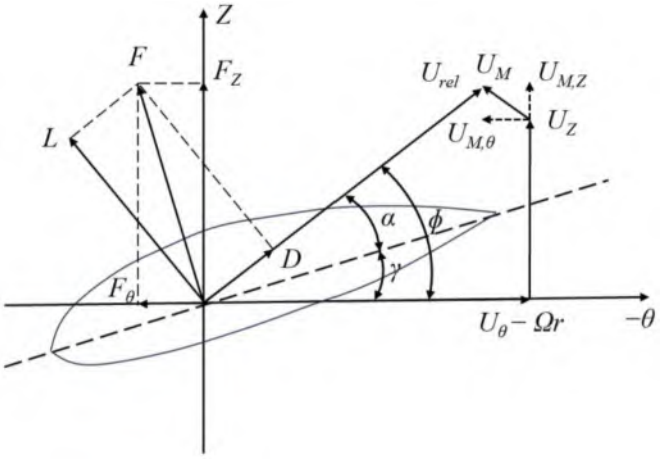

Fig. 1. Velocity vectors of the blade element.

and water, respectively, while values between 0 and 1 represent the interface between the two phases. The six-degree-of-freedom motions of the floating platform are solved by considering the hydrodynamic, aerodynamic, gravitational, and mooring forces and moments. The platform displacement and rotation are imposed on the body surface, and the surrounding mesh is deformed accordingly while maintaining its topology. The mesh velocity is incorporated into the governing equations to account for the moving control volumes. The updated platform position and mesh are subsequently used in the flow-field and aerodynamic calculations.

Wave generation and absorption are implemented using the numerical wave tank module of naoe-FOAM-SJTU (Cheng et al., 2019). First-order Stokes regular waves are generated by prescribing the theoretical free-surface elevation and water-particle velocities at the inlet. The corresponding expressions are given by:

$$\eta = A\cos(kx - \omega t) \tag{7}$$

$$\begin{cases} u = \dfrac{\pi H}{T}\dfrac{\cosh k(z+d)}{\sinh kd}\cos(kx-\omega t) \\ w = \dfrac{\pi H}{T}\dfrac{\sinh k(z+d)}{\sinh kd}\sin(kx-\omega t) \end{cases} \tag{8}$$

where, A and H are the wave amplitude and wave height; k and ω represent wave number and wave circular frequency; d denotes the water depth, and z represents vertical coordinate. To reduce wave reflection at the outlet, a sponge layer is employed, in which an artificial damping source term is added to the momentum equation:

$$\mathbf{f}_s = -\rho\mu_s\mathbf{U} \tag{9}$$

$$\mu_s = \begin{cases} \alpha_s\left(\dfrac{x-x_0}{L_S}\right)^2, & x > x_0 \\ 0, & x \le x_0 \end{cases} \tag{10}$$

where, μ_s represents the artificial viscosity; α_s denotes the damping strength coefficient; L_S is the length of sponge layer, and x_0 denotes the start point of the sponge layer. The damping strength increases toward the outlet, thereby attenuating the outgoing waves.

The mooring system is modeled using the piecewise extrapolating method (PEM), which is a quasi-static approach (Liu et al., 2017; Cheng et al., 2019). Each mooring line is divided into a number of segments, and the equilibrium equations are solved to determine the line configuration and tension. The submerged weight, line elongation, and hydrodynamic drag forces are considered, with the latter evaluated using Morison's equation. During the coupled simulation, wave-induced hydrodynamic loads and turbine aerodynamic loads drive the platform motions, which update the fairlead positions and the corresponding mooring-line configuration. The resulting mooring forces and moments are then transferred to the six-degree-of-freedom solver as restoring loads. Further details of the PEM and the coupling implementation can be found in Cheng et al. (2019).

2.4. Atmospheric turbulence inflow modeling

Atmospheric turbulent inflow is modeled using the precursor simulation approach to generate ABL conditions. The precursor simulations are performed using SOWFA (Churchfield et al., 2012), an open-source software developed by the National Renewable Energy Laboratory (NREL) based on OpenFOAM. Compared with synthetic turbulence inflow models, the precursor simulation approach provides turbulence inflow conditions that are more physically realistic, although it requires higher computational cost. SOWFA has been widely applied and validated in previous studies on wind turbine wakes (Churchfield et al., 2012; Ning and Wan, 2019; Yang et al., 2022).

In the precursor simulation stage, a rectangular computational domain without wind turbines is used. Cyclic boundary conditions are applied on the lateral boundaries, a slip boundary condition is imposed at the top boundary, and the Moeng boundary condition (Moeng, 1984) is prescribed at the bottom boundary. The flow is simulated using LES for a sufficiently long duration until a quasi-equilibrium ABL is established. Further details on atmospheric turbulence inflow modeling within the SOWFA framework can be found in Churchfield et al. (2012). After the flow field reaches a quasi-equilibrium state, the spatiotemporal data on the upstream plane are extracted and prescribed as the inflow condition for the air phase in the FOWT-UALM-SJTU solver to conduct fully coupled aero-hydro simulations of the FOWTs (Xu et al., 2024). Since the precursor simulation is used to provide the inflow boundary condition rather than being geometrically coupled with the FOWT computational domain, identical vertical extents are not required for the two domains. The precursor domain should cover the entire vertical range required by the air-phase inlet of the coupled domain.

3. Numerical simulation

3.1. Floating offshore wind turbine model

The wind turbine model adopted in this study is the reference NREL 5 MW (Jonkman et al., 2009). The rated wind speed of the turbine is 11.4 m/s, with a rotor diameter of 126 m and a hub height of 90 m. The floating support platform corresponds to Phase II of the OC4 project (Robertson et al., 2014), which is a semi-submersible platform with a draft of 20 m. The floating platform is moored by three mooring lines, which are symmetrically arranged around the platform center and configured as three catenary lines. The layout of the mooring system is shown in Fig. 2. The main parameters of the wind turbine and the floating platform are summarized in Table 1.

3.2. Atmospheric boundary layer inflow generation

The computational domain for the atmospheric boundary layer (ABL) simulation is illustrated in Fig. 3. The domain is a rectangular box with dimensions of 3000 m × 1000 m × 1000 m. A slip boundary

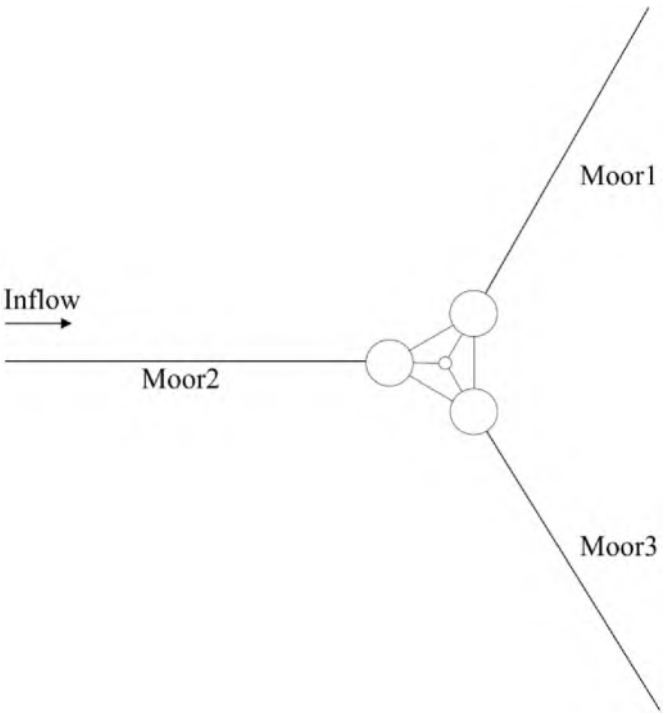

Fig. 2. The layout of the mooring system.

Table 1
Main parameters of the NREL 5 MW and the OC4 Phase II semi-submersible platform.

Parameters	Value
Number of blades	3
Rotor diameter (m)	126
Hub diameter (m)	3
Hub height (m)	90
Rated wind speed (m/s)	11.4
Rated rotor speed (rpm)	12.1
Rated power (MW)	5
Total mass (kg)	1.4×10^7
Total draft (m)	20
Total pitch inertia about center of mass (kg·m^2)	1.1×10^{10}
Total yaw inertia about center of mass (kg·m^2)	1.226×10^{10}
Total roll inertia about center of mass (kg·m^2)	1.1×10^{10}
Number of mooring lines	3
Mooring line diameter (m)	0.0766
Radius to anchors from center of rotation (m)	837.6
Unit mass under water (kg/m)	108.63

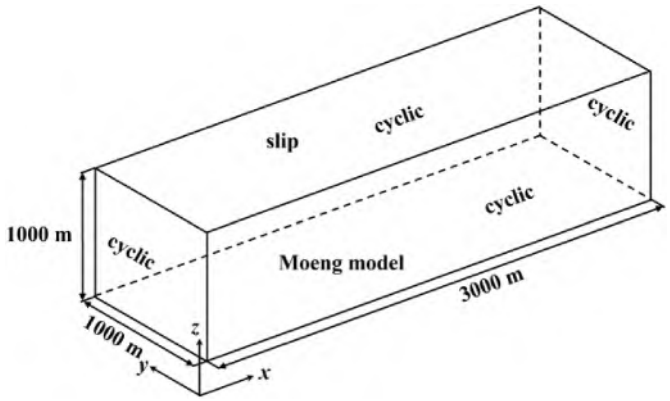

Fig. 3. The computational domain for the ABL simulation.

condition is applied at the top boundary, the Moeng boundary condition (Moeng, 1984) is imposed at the bottom boundary, and cyclic boundary conditions are prescribed at the lateral boundaries. The mean wind speed at hub height (90 m) is set to $U_0 = 11.4$m/s, and the surface roughness length is specified as 0.001 m, representing a typical offshore environment (Churchfield et al., 2012). The Coriolis acceleration is included in the momentum equation, while the background pressure gradient is dynamically adjusted to maintain the prescribed mean wind speed at hub height (Churchfield et al., 2012). When the generated ABL is used as the inflow condition for the two-phase flow simulations, a reduced vertical grid spacing near the bottom boundary is required (Xu et al., 2024). Therefore, the grid spacing in the x and y directions is set to 10 m, while a vertically stretched grid with linear growth is adopted in the z direction. The vertical grid size at the bottom boundary is 0.24 m. In previous studies, computational domains and grid resolutions of similar scales have been demonstrated to be sufficient for capturing the turbulent structures of the ABL (Churchfield et al., 2012; Ning and Wan, 2019; Xu et al., 2024). An initial simulation is performed using a time step of 0.2 s with a total duration of 18,000 s to achieve a quasi-equilibrium ABL. Subsequently, the simulation is continued for an additional 600 s with a reduced time step of 0.02 s, and the resulting flow field is used as the inflow condition for the coupled FOWT simulations. The recorded precursor data are spatially mapped onto the air-phase inlet boundary of the coupled FOWT domain. Since the time step of the coupled FOWT simulation is 0.01 s, the inlet values at intermediate time levels are obtained by linear temporal interpolation between two consecutive precursor snapshots.

Fig. 4 presents the horizontal-plane-averaged vertical profiles of wind speed and turbulence intensity in the precursor ABL. The upper, middle, and lower dashed lines denote the highest blade-tip position, the hub center, and the lowest blade-tip position, respectively. The wind speed profile is normalized by the mean wind speed at hub height. The results indicate that the mean wind speed at hub height matches the rated wind speed of 11.4 m/s, and the vertical wind-speed variation can be reasonably approximated by a power-law profile over the height range of interest. The estimated wind shear exponent is approximately 0.11. The turbulence intensity decreases with increasing height, and the turbulence intensity at hub height is approximately 7.35%. Fig. 5 shows the power spectral density (PSD) of the wind speed fluctuations at hub height. It can be observed that, over part of the inertial subrange, the PSD approximately follows the −5/3 scaling, indicating that the inertial

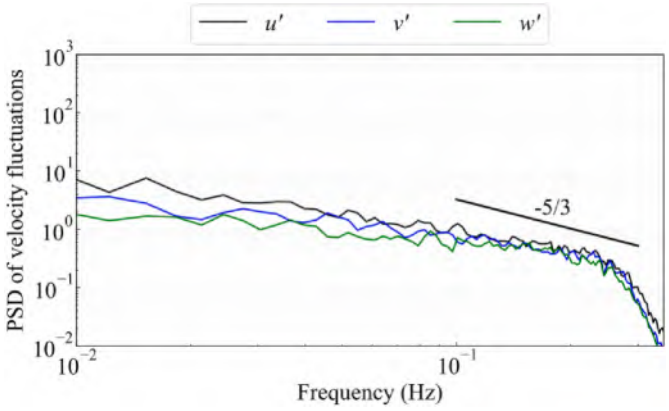

Fig. 5. The PSD of the wind speed fluctuations at hub height.

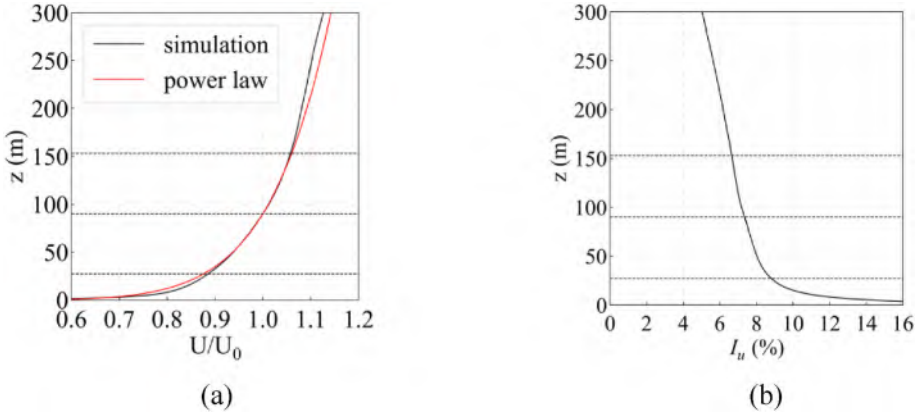

Fig. 4. The time-averaged vertical profiles: (a) wind speed; (b) turbulence intensity.

subrange is well resolved (Churchfield et al., 2012). This further confirms the reliability of the simulated ABL.

To further examine whether the ABL characteristics are maintained after the inflow data are transferred to the two-phase computational domain, an additional wind-field propagation simulation without wind turbines is performed. The same ABL inflow treatment as that used in the coupled FOWT simulations is adopted, and the probes are arranged at three streamwise locations, approximately $x/D = 3$, 6, and 10 from the inlet. The statistics are calculated over 600 s using the velocity time series at corresponding probe locations in both the precursor and wind-field simulations. Fig. 6 compares the vertical profiles of the mean streamwise velocity and streamwise turbulence intensity. The overall shapes of the vertical profiles are retained after the inflow is transferred to the two-phase computational domain, although systematic differences in their magnitudes are observed. The overall vertical distributions of both quantities remain similar at the three streamwise locations. The mean streamwise velocity in the wind-field simulation is approximately 2.5%-2.6% higher than that in the precursor ABL, whereas the streamwise turbulence intensity is reduced by approximately 0.64-0.89 percentage points. This difference is likely associated with the different lower-boundary treatments in the precursor and two-phase computational domains. Moreover, no pronounced further decay of turbulence intensity is observed from $x/D = 3$ to $x/D = 10$, indicating that the transferred turbulent wind field remains relatively stable during downstream propagation.

3.3. Numerical setup

The coupled FOWT simulations are performed using the in-house solver FOWT-UALM-SJTU, which has been extensively validated under various operating conditions in previous studies (Cheng et al., 2019; Huang et al., 2023; Wang et al., 2019; Xu et al., 2024). The computational domain for the coupled FOWT simulations is shown in Fig. 7, where all distances are normalized by the wind turbine rotor diameter D. Two streamwise spacings of 5D and 7D are considered between the two FOWTs. Regular wave conditions are considered in this study, with a wave height of 7.58 m and a wave period of 12.1 s, and the wave propagates along the positive x-direction. The first FOWT is located 350 m downstream of the inlet, corresponding to approximately 1.5 wavelengths. The water depth is 200 m. The height of the air domain is 320 m (approximately 2.54D), which is sufficient to allow the development of the wind turbine wake. A wave damping zone with a length of 460 m is arranged upstream of the outlet boundary.

The boundary conditions are specified as follows. The combined wind-wave inflow is prescribed at the inlet, where the inflow wind field is provided by the generated ABL. A zero-gradient boundary condition is applied at the outlet. The slip boundary conditions are imposed at the top and bottom boundaries, while symmetry boundary conditions are used at the lateral boundaries.

The mesh configuration of the computational domain and the local mesh deformation around the floating platform are illustrated in Fig. 8. In the upstream region of the FOWTs and in the wake region, the background grid spacing in the x and y directions is 10 m. The grid size in the z direction reaches 2.5 m near the free surface and 10 m in the wake region. To satisfy the requirements for free-surface capturing and wake evolution, secondary mesh refinement is applied near the free surface and within the wake region. After refinement, the vertical grid size near the free surface is reduced to 0.625 m, which is approximately one-twelfth of the wave height, while the grid spacing in the wake region is refined to 2.5 m in all three directions. In addition, local mesh refinement is applied around the floating platform to accurately resolve the hydrodynamic responses. To reduce mesh complexity and computational cost, the cross braces are omitted in the simulations, as previous studies have demonstrated that their influence on the simulation results is negligible (Li et al., 2023). The total number of cells is approximately 17 million. The simulations are performed with a time step of 0.01 s, and the total simulation duration corresponds to approximately 50 wave periods to ensure statistically stable results.

To investigate the aerodynamic performance and wake characteristics of FOWTs under partial wake conditions, ten cases involving two FOWTs under different wake configurations are simulated. The upstream turbine is denoted as WT0, while the downstream turbine is denoted as WT1. Two streamwise spacings of 5D and 7D are considered, while the lateral offset between WT1 and WT0 is varied from 0D to 1D. These streamwise spacings are selected to represent two typical configurations within the commonly adopted inter-turbine spacing range of approximately 5D-10D in wind farm arrays (Sant, 2026). The schematic illustration of the considered cases is shown in Fig. 9, where Δx and Δy denote the streamwise spacing and lateral offset between WT0 and WT1, respectively. The corresponding normalized layout parameters of Cases 1 to 10 are summarized in Table 2. Specifically, Cases 1 to 5 correspond to a streamwise spacing of 5D with lateral offsets of 0D, 1/4D, 1/2D, 3/4D, and 1D, respectively, while Cases 6 to 10 adopt a streamwise spacing of 7D with the same sequence of lateral offsets. Cases 1 and 6 represent the fully waked conditions, whereas the remaining cases correspond to partial wake conditions with increasing lateral offset.

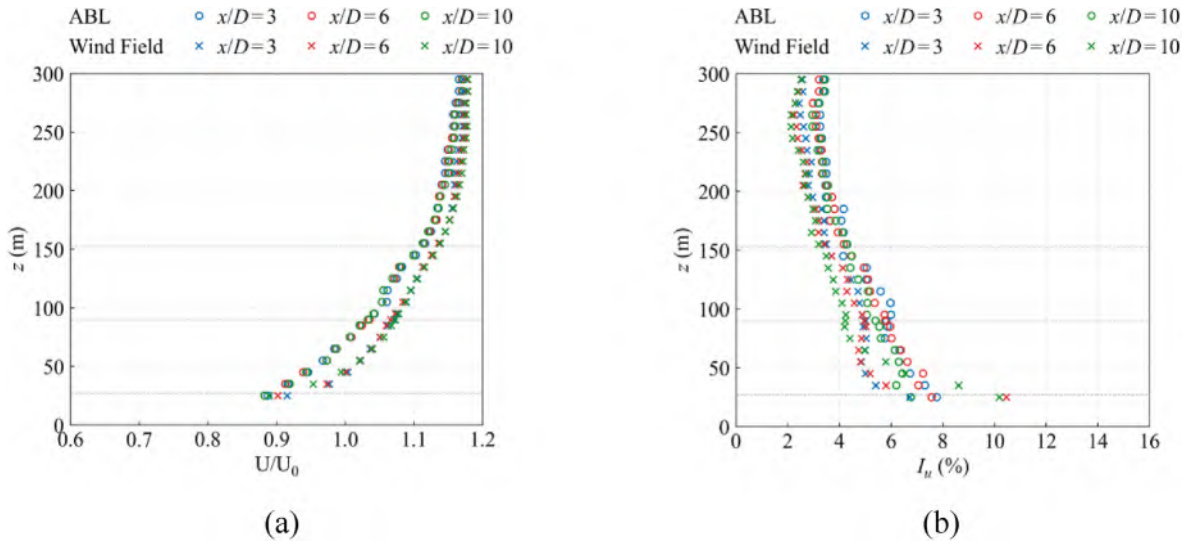

Fig. 6. Comparison of the vertical profiles between the precursor ABL and the wind-field simulation: (a) wind speed; (b) turbulence intensity.

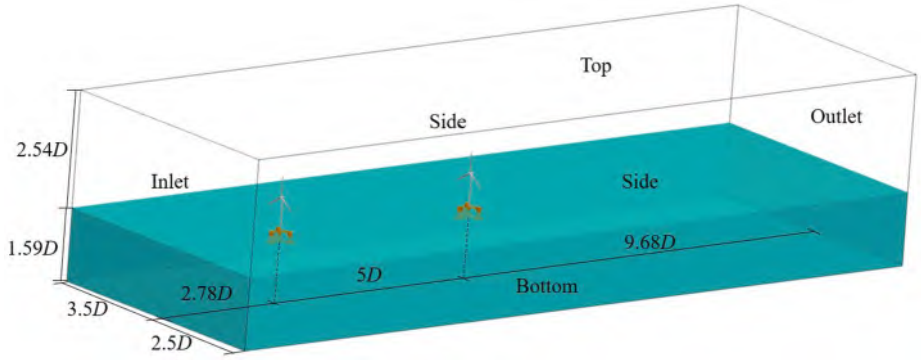

Fig. 7. The computational domain for the coupled FOWT simulations.

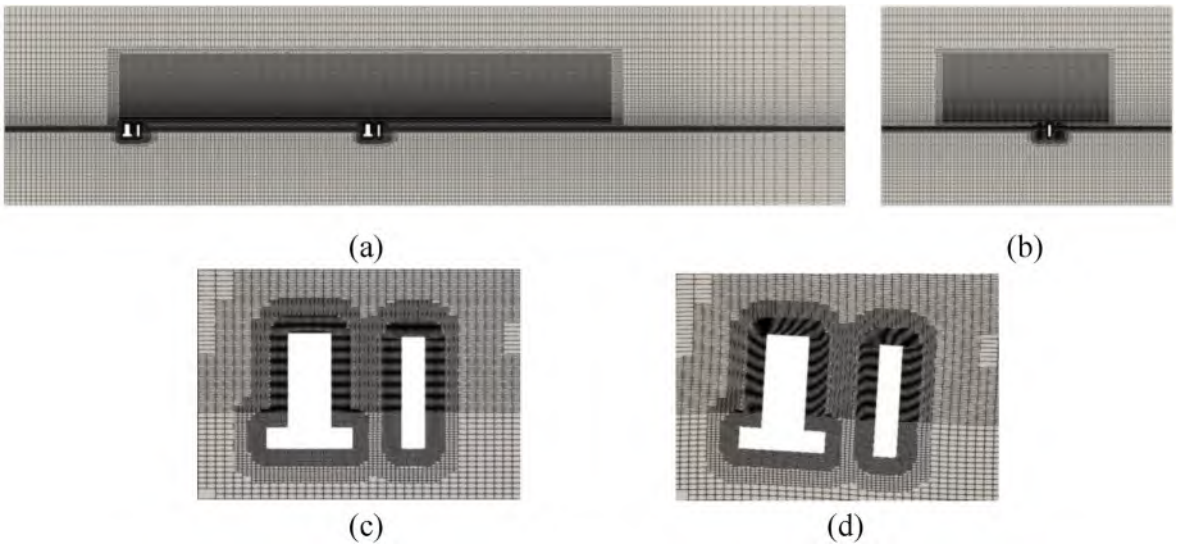

Fig. 8. Mesh configuration and deformation: (a) xz plane; (b) yz plane; (c) initial mesh around the floating platform; (d) deformed mesh around the floating platform at a representative instant.

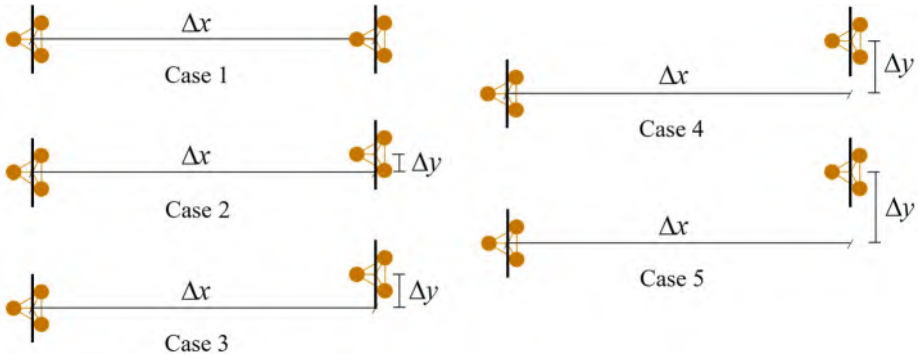

Fig. 9. Schematic illustration of the lateral-offset configurations for the 5D streamwise spacing.

3.4. Mesh and time-step convergence study

To verify the adequacy of the selected mesh resolution and time step for the aerodynamic and wake simulations, a mesh and time-step convergence study is performed. The convergence cases adopt the same tandem configuration as Case 1, with both turbines fixed, while all other numerical settings remain identical to those of Case 1. To ensure statistical stability, the results are analyzed over the last ten wave periods of the simulations. For the mesh convergence study, three computational meshes with different resolutions are designed. In the wake region, the mesh spacing is kept uniform in the *x*-, *y*-, and *z*-directions, with mesh sizes of 3 m, 2.5 m, and 2 m, corresponding to the coarse, medium, and fine meshes, respectively. Fig. 10 presents the time histories of power and thrust for the two wind turbines under different mesh resolutions, where time is normalized by the wave period. Compared with the fine mesh, the power and thrust predicted using the coarse mesh are slightly underestimated, whereas the results obtained with the medium mesh agree well with those of the fine mesh. This

Table 2
Normalized layout parameters of cases.

Cases	$\Delta x/D$	$\Delta y/D$
1	5	0
2	5	1/4
3	5	1/2
4	5	3/4
5	5	1
6	7	0
7	7	1/4
8	7	1/2
9	7	3/4
10	7	1

indicates that mesh convergence is achieved when the mesh resolution reaches the medium level. Considering both computational accuracy and computational cost, the medium mesh is adopted in the subsequent coupled simulations.

For the time-step convergence study, the medium mesh determined above is employed, and three time-step sizes, 0.0125 s, 0.01 s, and 0.0075 s, are considered. Fig. 11 shows the time histories of power and thrust of the two wind turbines under different time steps. The results demonstrate that both the variation trends and amplitudes of power and thrust are nearly identical for the different time steps, indicating that the results are converged with respect to the time-step size. Consequently, a time step of 0.01 s is selected for the simulations.

To further assess the mesh independence of the hydrodynamic responses of the floating platform, an additional mesh convergence study is conducted under wave-only conditions using a single floating platform without aerodynamic loading. Three mesh resolutions, namely coarse, medium, and fine meshes, are considered, while the wave conditions and other numerical settings are kept unchanged. The corresponding grid spacings near the free surface in the x-, y-, and z-directions are approximately (3.125, 3.125, 0.833) m, (2.5, 2.5, 0.625) m, and (2.0, 2.0, 0.5) m for the coarse, medium, and fine meshes, respectively. Fig. 12 compares the time histories of surge, heave, and pitch motions under different mesh resolutions. The results obtained with the medium mesh agree well with those of the fine mesh, while slightly larger deviations are observed for the coarse mesh. This confirms that the medium mesh provides sufficient accuracy for predicting the hydrodynamic motion responses of the floating platform.

4. Results and discussion

4.1. Inflow characteristics

The inflow characteristics of the downstream turbine WT1 under partial wake conditions are first analyzed. Since WT1 is located within the wake-affected region of the upstream turbine WT0, significant differences arise in the inflow velocity distribution and its non-uniformity under different lateral offset cases. To ensure statistical reliability, the time-averaged flow field over approximately the last ten wave periods is used for comparison, and a cross-sectional plane located 1D upstream of WT1 is selected to represent the inflow conditions. Fig. 13 presents the time-averaged velocity contours on this inflow plane for Cases 1 to 5 with a streamwise spacing of 5D, where the black dashed circle denotes the projected rotor disk of WT1 on the section. As the lateral offset varies, the velocity distribution within the projected rotor area changes markedly. For small lateral offsets, WT1 remains largely within the wake region of WT0, resulting in an overall reduced inflow velocity with a relatively uniform distribution. As the lateral offset increases, the projected rotor disk gradually enters a partial wake state, and stronger non-uniformity of velocity is observed across the rotor disk. As the lateral

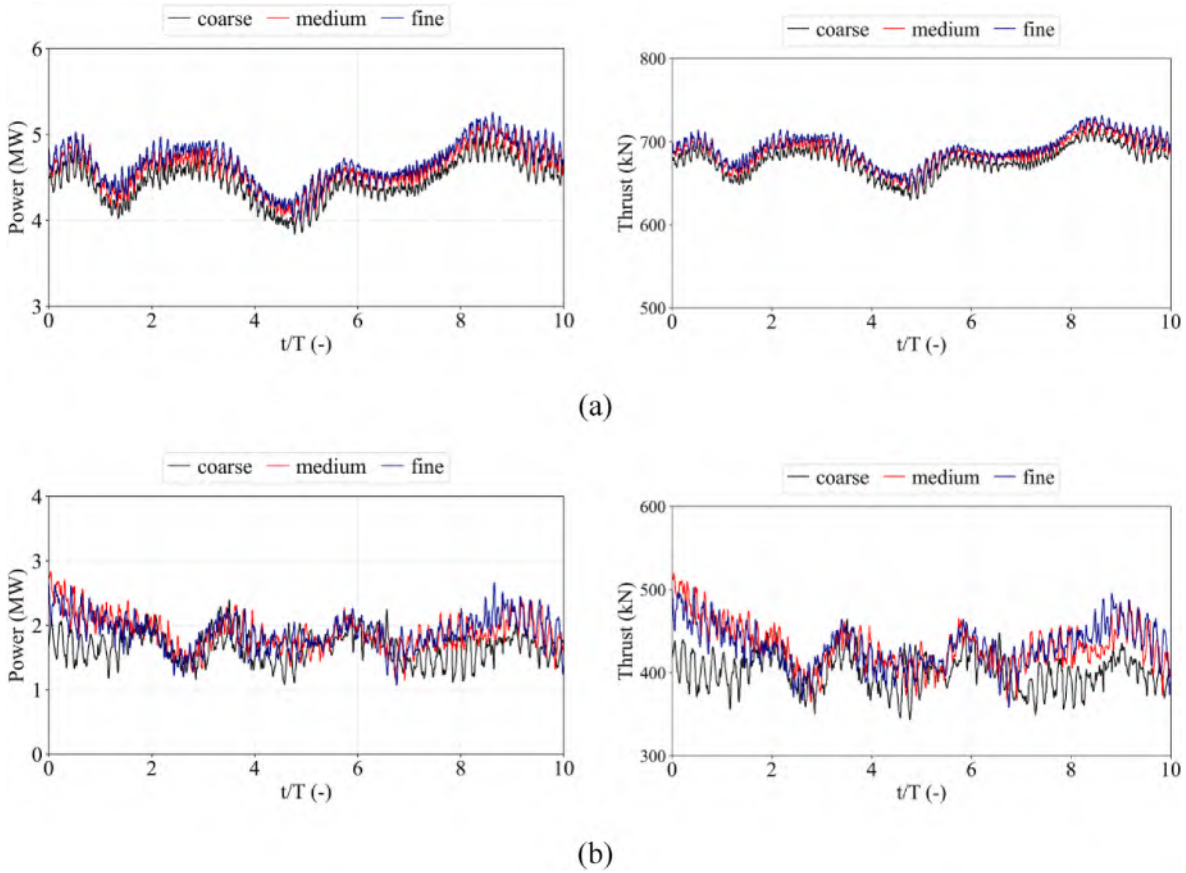

Fig. 10. The time histories of power and thrust for the two wind turbines under different mesh resolutions: (a) WT0; (b) WT1.

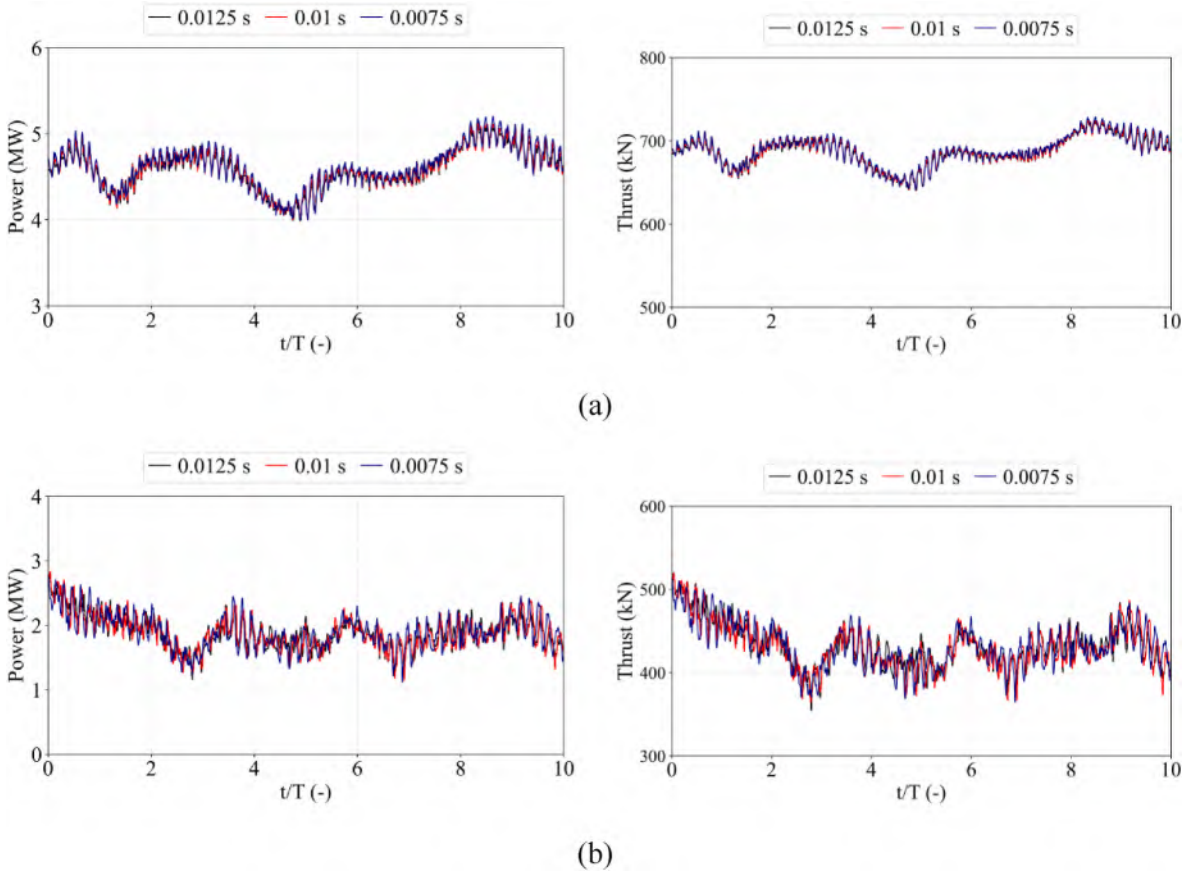

Fig. 11. The time histories of power and thrust for the two wind turbines under different time steps: (a) WT0; (b) WT1.

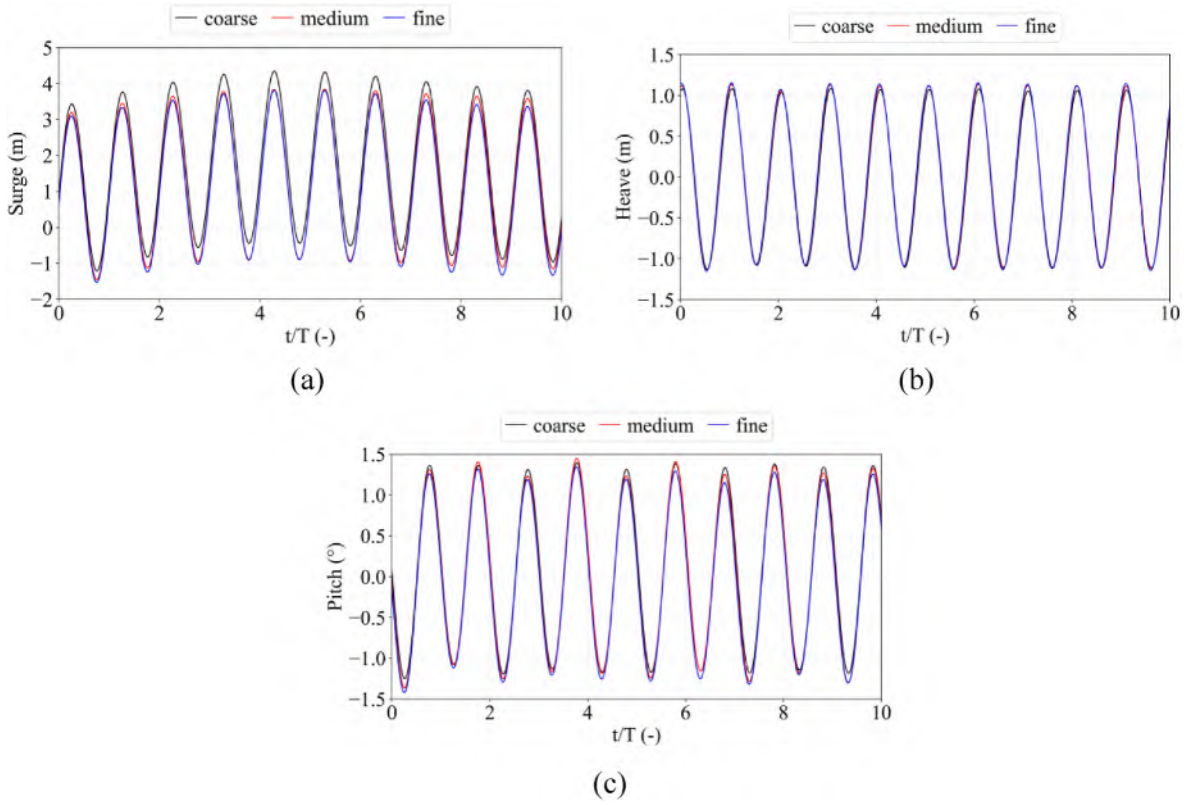

Fig. 12. The time histories of platform motions under different mesh resolutions: (a) surge; (b) heave; (c) pitch.

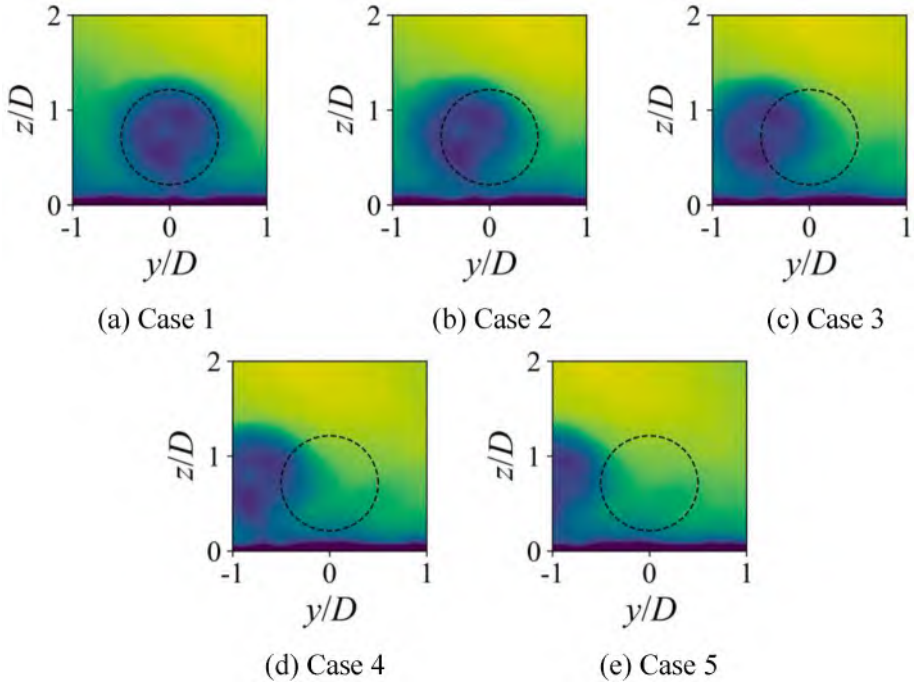

Fig. 13. Time-averaged inflow velocity contours on the plane located 1*D* upstream of WT1.

offset increases further, WT1 progressively moves out of the upstream wake influence, and the inflow velocity level recovers and approaches a more uniform distribution. A similar variation in the inflow characteristics is also observed for the cases with a streamwise spacing of 7*D*, as further quantified below. These variations in inflow characteristics directly affect the aerodynamic performance and subsequent wake evolution of WT1.

To further quantify the inflow differences of WT1 under different cases, several representative inflow metrics within the projected rotor disk of WT1 are evaluated, as summarized in Table 3. The statistical quantities include the rotor-averaged mean velocity, the mean velocities of the left and right half-disks, and the spatial standard deviation of velocity over the rotor disk. For the cases with a streamwise spacing of 5*D*, the results indicate that, as the lateral offset increases from 0*D* to 1*D*, the rotor-averaged inflow velocity of WT1 exhibits an overall increasing trend. The non-uniformity of the disk velocity is significantly enhanced during the partial wake stage. Compared with Case 1, the difference between the right- and left-half mean velocities and the spatial standard deviation in Cases 2 and 3 increase markedly, indicating the presence of pronounced lateral inflow non-uniformity across the rotor disk. As the lateral offset further increases to 1*D*, both the left-right velocity difference and the spatial standard deviation gradually decrease, suggesting that the inflow non-uniformity of WT1 is substantially alleviated and tends to recover. The cases with a streamwise spacing of 7*D* show a similar dependence on lateral offset: the rotor-averaged inflow velocity generally increases with increasing lateral offset, while the inflow non-uniformity is most pronounced at intermediate offsets and decreases as WT1 moves further out of the upstream wake. In particular, the maximum spatial standard deviation decreases from 1.65 m/s in Case 3 to 1.20 m/s in Case 8, indicating that the additional downstream distance allows further wake recovery and mixing before the wake reaches WT1. Overall, Cases 1 and 6 represent the fully wake-covered conditions for the 5*D* and 7*D* streamwise spacings, respectively, where the rotor-averaged inflow velocity is relatively low and its spatial distribution is comparatively uniform. For both streamwise spacings, the intermediate lateral offsets correspond to more representative partial wake conditions with stronger inflow non-uniformity, whereas the wake influence is gradually weakened at larger lateral offsets and the inflow conditions progressively approach the free-stream state.

Table 3
Rotor-disk inflow statistics of WT1.

Cases	Rotor-averaged mean (m/s)	Left-half mean (m/s)	Right-half mean (m/s)	Spatial STD over disk (m/s)
1	8.06	7.99	8.12	0.66
2	8.69	7.71	9.66	1.33
3	9.84	8.46	11.18	1.65
4	11.05	10.28	11.81	1.27
5	11.69	11.45	11.92	0.74
6	8.87	8.50	9.24	0.64
7	9.49	8.64	10.33	1.10
8	10.40	9.45	11.34	1.20
9	11.29	10.78	11.79	0.97
10	11.74	11.55	11.94	0.74

4.2. Motion responses

This subsection examines the platform motion responses of the downstream turbine WT1 under different partial wake conditions. To ensure statistical reliability, the results over approximately the last ten wave periods are selected for comparison. Fig. 14 presents the time histories of the 6-DOF motions of WT1 under different cases. Among all motion components, surge and pitch exhibit relatively large response amplitudes, and these two degrees of freedom are therefore taken as the main focus in the following analysis. The cases with a streamwise spacing of 7*D* exhibit similar overall motion characteristics, with surge and pitch remaining the dominant response components. This is consistent with the conclusions drawn from the previous inflow analysis, namely that, as the inflow velocity of WT1 increases, the mean thrust level also increases, leading to more pronounced surge and pitch responses. In contrast, the differences in heave motion among the cases are relatively small, indicating that the heave response is mainly governed by the hydrodynamic characteristics of the platform and the wave conditions, while the influence of aerodynamic load variation remains limited. For sway, roll, and yaw, the motion amplitudes remain generally small under the present conditions, and their direct influence on the subsequent aerodynamic and wake characteristics is therefore expected

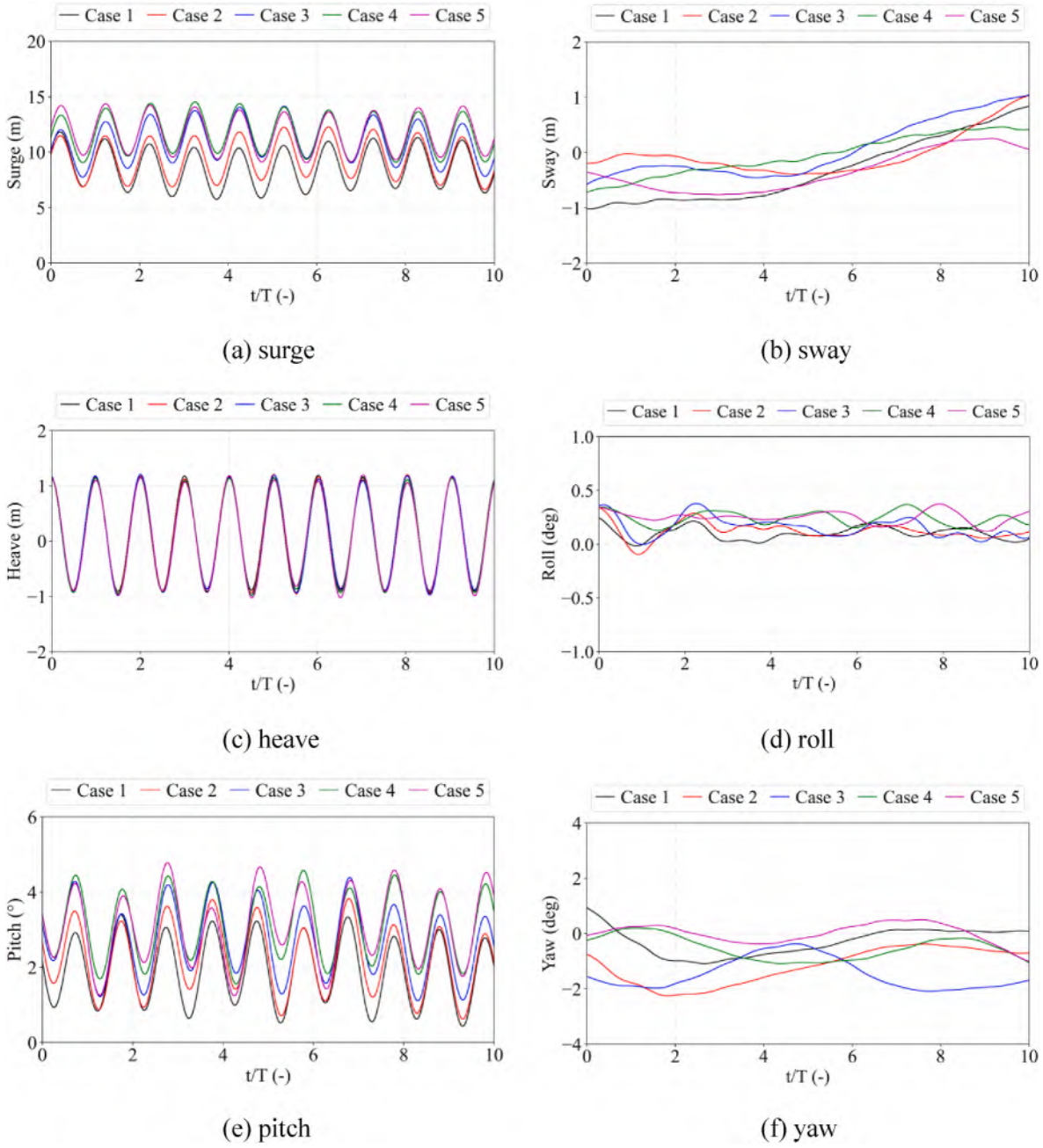

Fig. 14. Time histories of the 6-DOF motions of WT1.

to be limited. It is worth noting that the mean yaw response in Case 3 is relatively larger than that in the other cases. This may be associated with the asymmetric aerodynamic loading induced by the partial wake.

Fig. 15 presents the statistical results of the surge and pitch motions of WT1 under different cases, including the time-averaged values and standard deviations, where the black dashed lines indicate the corresponding values of WT0 for reference. In the horizontal-axis labels, "C" denotes "Case". For each paired group, the left and right bars correspond to the 5*D* and 7*D* streamwise spacings, respectively. The results show that the influence of partial wake conditions on the fluctuation intensities of surge and pitch is relatively limited, and only small differences are observed among the cases. This indicates that the platform motion fluctuations are still mainly governed by wave excitation, whereas the influence of the partial wake is reflected more in the mean response level than in the fluctuation intensity. By contrast, the differences in the mean values are more pronounced. As the lateral offset increases, WT1 gradually moves away from the central region of the wake, and the rotor-averaged inflow velocity continuously increases. As a result, the mean thrust also increases, leading to gradually larger mean offsets in surge and pitch. For the larger lateral-offset cases at both streamwise spacings, the mean motion responses of WT1 gradually approach those of WT0 under free-stream inflow conditions. The 7*D* cases show the same overall dependence on lateral offset, indicating that the relationship between inflow recovery, mean aerodynamic loading, and the mean surge and pitch responses is maintained as the streamwise spacing increases. Overall, the partial wake not only alters the inflow conditions of WT1, but also affects its platform motion responses. The aerodynamic performance of WT1 under different partial wake conditions is further analyzed in the following section.

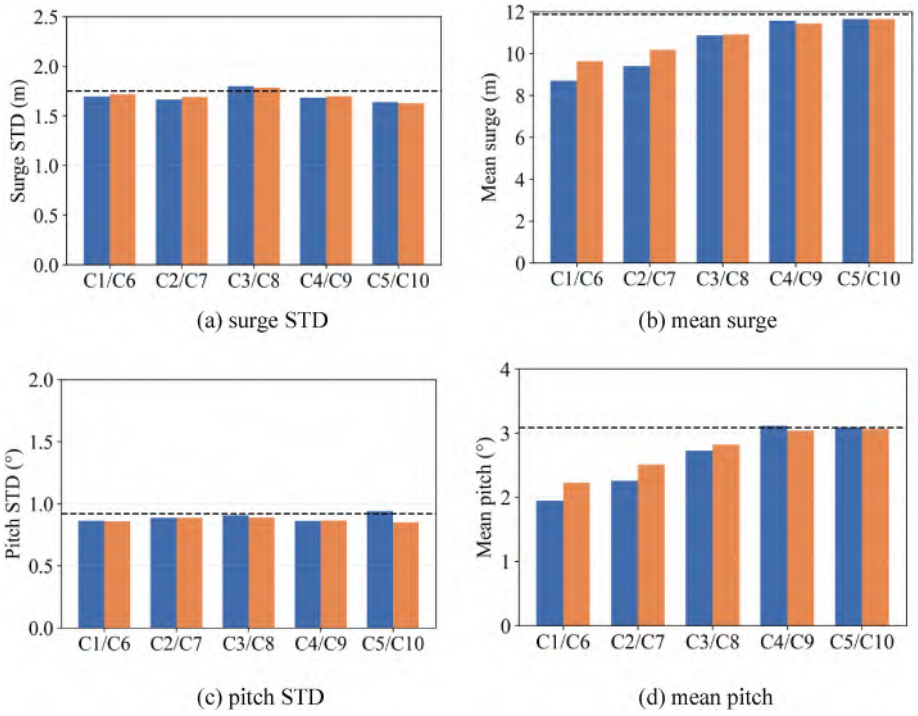

Fig. 15. Time-averaged values and STD of the surge and pitch motions of WT1, with dashed lines indicating the corresponding values of WT0.

4.3. Aerodynamic characteristics

Aerodynamic characteristics are important for assessing the operational state of a FOWT and the impact of wake effects. In this section, the aerodynamic characteristics of the downstream turbine WT1 under partial wake conditions are analyzed. To ensure statistical reliability, the data over the last ten wave periods of the simulations are used for analysis. Fig. 16 presents the time histories of thrust and power of WT1 for Cases 1 to 5 with a streamwise spacing of 5*D*. Overall, pronounced fluctuations are observed in both thrust and power under all cases. This is mainly because the inflow of WT1 is simultaneously affected by ABL turbulence and the wake of the upstream turbine, resulting in strong temporal and spatial non-uniformity of the inflow. For the cases located within the wake region of the upstream turbine, the wake velocity deficit reduces the inflow velocity over the rotor disk, thereby decreasing the time-averaged thrust and power of the wind turbine. A comparison among the different cases shows that the thrust and power of WT1 generally follow the trend of the inflow velocity distribution. Specifically, Case 1, which is located within the fully waked region, yields the lowest thrust and power because it is subjected to the strongest velocity deficit. As the lateral offset of WT1 increases, the inflow condition is gradually improved, and the thrust and power increase accordingly. The cases with a streamwise spacing of 7*D* exhibit the same overall dependence on lateral offset, as further demonstrated by the statistical results below.

Fig. 17 further compares the statistical results of thrust and power under different cases, including the time-averaged values and standard deviations, where the dashed lines denote the corresponding results of WT0. It is found that the time-averaged thrust and power of WT1 gradually increase as the wake influence weakens. For the larger lateral-offset cases at both streamwise spacings, the mean thrust and power of WT1 become comparable to, or even slightly higher than, those of WT0 as the wake influence is substantially weakened. This is likely because the ABL inflow is inherently non-uniform, and the local mean inflow velocity at the WT1 position in these cases may be slightly higher than that at WT0. Nevertheless, for the time-averaged aerodynamic performance, the wake velocity deficit remains the dominant factor governing the differences among the cases. In contrast to the variation trend of the

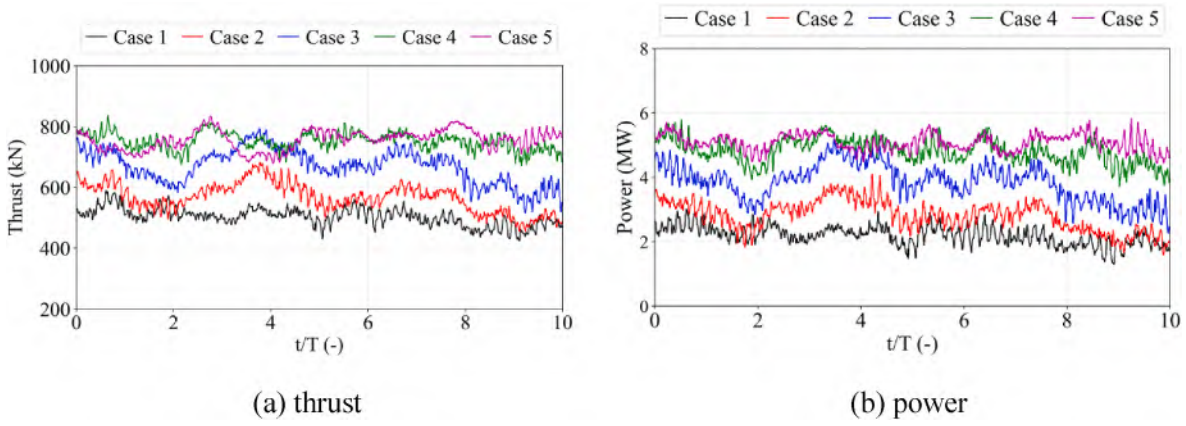

Fig. 16. Time histories of thrust and power of WT1.

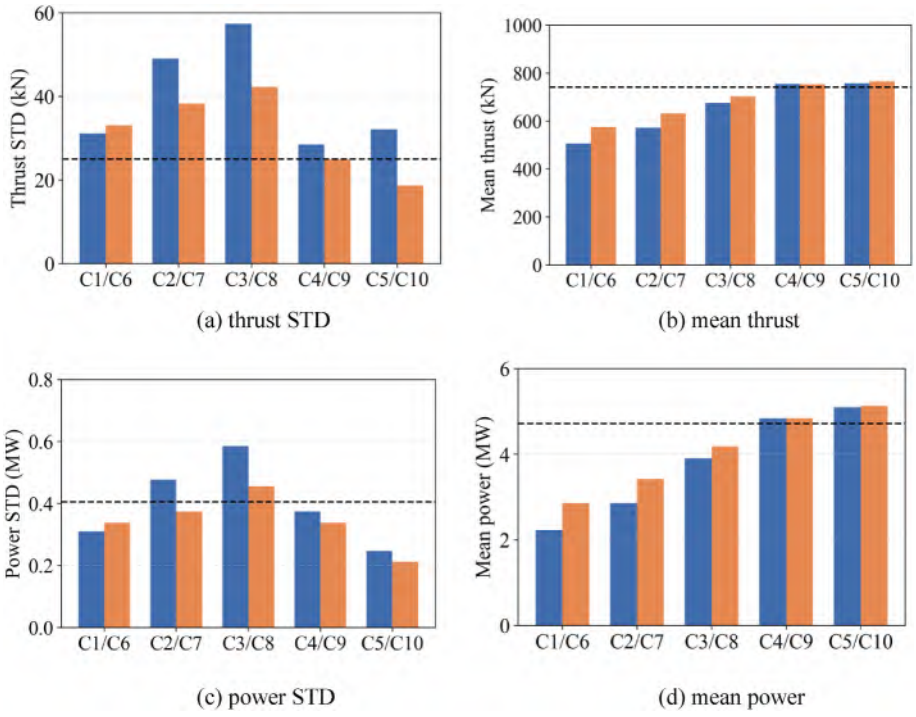

Fig. 17. Time-averaged values and STD of thrust and power of WT1, with dashed lines indicating the corresponding values of WT0.

mean values, the fluctuation intensities of thrust and power become more pronounced under partial wake conditions. For the 5*D* cases, the most significant fluctuations occur in Case 3, followed by Case 2, while the 7*D* cases exhibit the same overall dependence on lateral offset, with stronger fluctuations occurring at intermediate offsets. However, for the corresponding lateral offsets, the standard deviations of thrust and power at the 7*D* spacing are noticeably lower than those at 5*D*. This is consistent with the lower spatial standard deviation of the WT1 inflow observed for the 7*D* cases, indicating that the enhanced wake recovery at the larger streamwise spacing reduces the inflow non-uniformity and consequently weakens the aerodynamic fluctuations. This indicates that stronger unsteady responses occur under partial wake conditions. The main reason is that the rotor is located near the boundary between the wake core region and the free-stream region. Under this condition, the rotor disk is simultaneously affected by the low-velocity wake and the higher-velocity free stream, resulting in a more uneven load distribution across the rotor disk. Meanwhile, wake meandering causes this non-uniform inflow to vary with time, thereby inducing stronger fluctuations in thrust and power. By contrast, under the fully waked condition, although the mean inflow velocity is lower, the entire rotor is located in a relatively uniform low-velocity region, and the inflow non-uniformity is therefore weaker. For the cases approaching free-stream inflow, the wake disturbance is already significantly reduced, and the corresponding unsteady responses are also weakened. Stronger thrust fluctuations imply enhanced unsteadiness of the axial load acting on the turbine, which may aggravate structural load variations and adversely affect the operational stability of the turbine. At the same time, large power fluctuations also reduce the stability of power output. Therefore, in the layout design of floating wind farms, attention should be paid not only to the mean power loss, but also to the enhanced unsteady loads induced by partial wake conditions.

Angle of attack (AOA) is a key parameter for characterizing the local aerodynamic state of the blade. Fig. 18 presents the spatiotemporal distributions of AOA along the blade span for WT0 and WT1 under different cases. For the upstream turbine WT0, the AOA exhibits a relatively regular periodic variation with time, while the overall fluctuation amplitude remains limited. This indicates that the aerodynamic states of the blade sections remain generally stable under free-stream inflow conditions. By contrast, the unsteadiness of AOA for WT1 is significantly enhanced in Cases 1, 2, and 3, as reflected by the periodic emergence of low-AOA regions along the blade span. Among these cases, the most significant variation is observed in Case 3, followed by Case 2, indicating that under stronger partial wake interference, a large portion of the blade periodically experiences a substantial decrease in AOA, with the local AOA occasionally approaching 0°. This suggests that the velocity deficit of the upstream wake and its meandering substantially alter the local inflow conditions of WT1, thereby leading to stronger time-varying fluctuations in the local aerodynamic states of the blade. This is consistent with the previously observed stronger fluctuations in thrust and power in Cases 2 and 3. By comparison, as the lateral offset of WT1 increases, the AOA distributions in Cases 4 and 5 gradually recover to levels close to those of WT0, indicating that the wake interference is significantly weakened and the blade aerodynamic state becomes more stable. The cases with a streamwise spacing of 7*D* exhibit the same overall dependence on lateral offset, with enhanced AOA unsteadiness under partial-wake conditions.

The out-of-plane blade-root bending moment (MOoP) is an important indicator for evaluating the structural loading and operational safety of wind turbines. Fig. 19 presents the time histories of MOoP for WT1 under Cases 1 to 5 with a streamwise spacing of 5*D*. Table 4 further summarizes the statistical results of MOoP together with the normalized damage equivalent load (DEL), where the DEL is normalized by the corresponding value of WT0. The DEL is a commonly used indicator for evaluating fatigue load levels, and it is usually calculated by identifying load cycles from the load time series using the rainflow counting method and then assessing cumulative damage based on the S-N curve (Kang and Lee, 2024). It should be noted that, because the time series used for DEL calculation in the present study is relatively short, greater emphasis is placed on comparing the relative variation pattern of DEL under different partial wake conditions rather than on making a strict prediction of turbine fatigue life. As shown in Fig. 19, under the combined influence of ABL turbulence and the wake of the upstream turbine, pronounced unsteady fluctuations of MOoP are observed for WT1 in all cases. Among them, the strongest fluctuations occur in Cases 2 and 3,

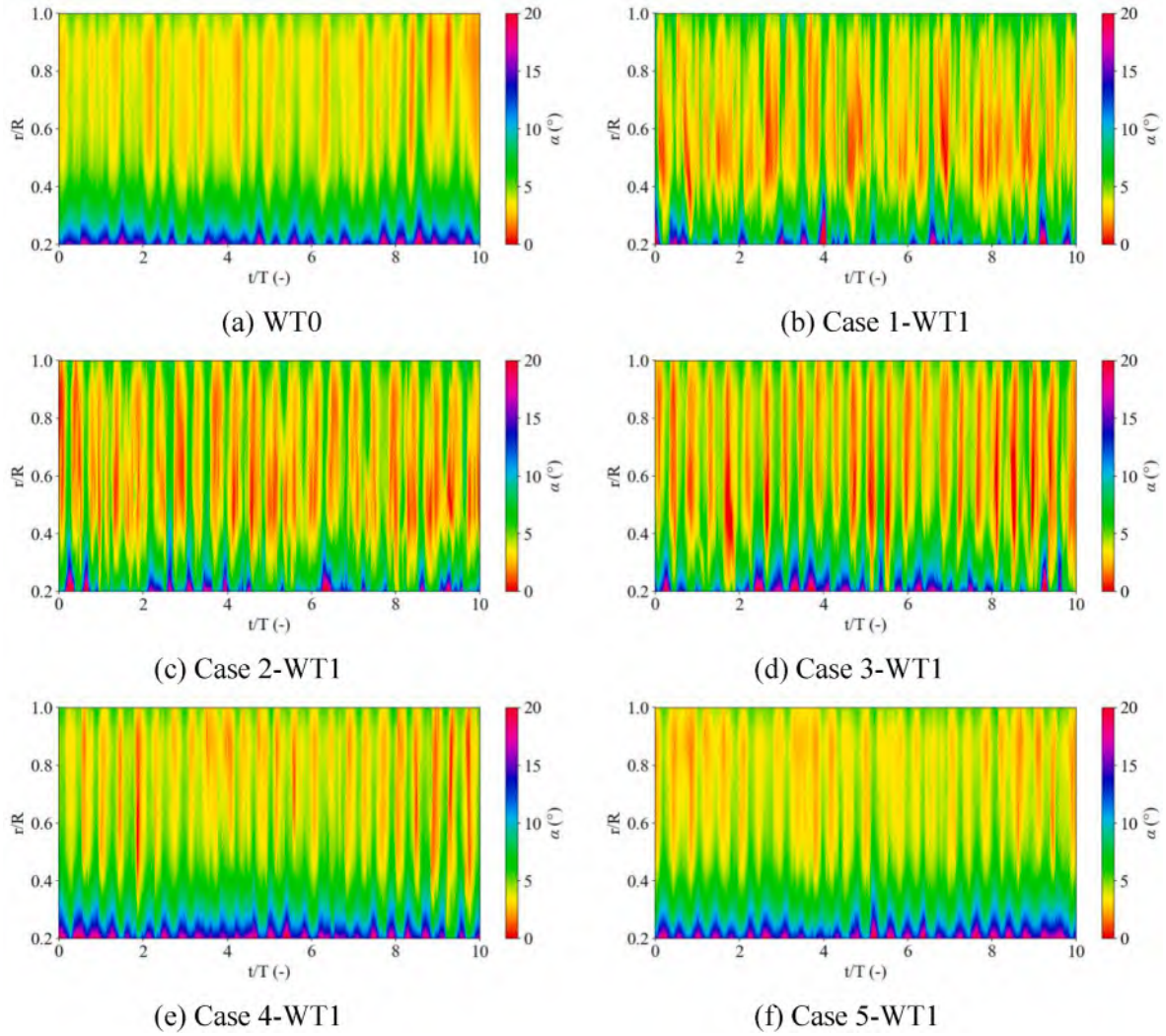

Fig. 18. Spatiotemporal distributions of the AOA along the blade span for WT0 and WT1 under different partial wake conditions.

whereas relatively weaker fluctuations are observed in Case 1, which is located in the fully waked region, and in Case 5, which has the largest lateral offset. This indicates that stronger inflow non-uniformity over the rotor disk is induced under partial wake conditions, thereby leading to more pronounced fluctuations of the blade-root bending moment. By contrast, under the fully waked condition, although the mean inflow velocity is lower, the entire rotor remains within a relatively uniform low-velocity region, and the inflow non-uniformity is therefore weaker, resulting in lower load fluctuations. In Case 5, as the wake influence is further reduced, the unsteadiness of MOoP also decreases accordingly. A similar dependence on lateral offset is observed for the 7*D* cases. The MOoP standard deviation increases under intermediate partial-wake conditions and subsequently decreases as WT1 moves further away from the wake core. Compared with the corresponding 5*D* cases, the MOoP fluctuations at the 7*D* spacing are generally weaker, consistent with the reduced inflow non-uniformity discussed previously. In terms of the mean value, the variation of MOoP generally follows the same trend as the inflow velocity and the corresponding aerodynamic thrust, that is, a higher mean inflow velocity leads to a larger bending moment acting on the blade. The DEL results show a similar overall dependence on lateral offset. For the 5*D* cases, Case 3 exhibits the largest normalized DEL, approximately 45% higher than that of the fully waked Case 1. For the 7*D* cases, the DEL is also elevated under intermediate partial-wake conditions, although Case 7 shows a slightly higher value than Case 8. This small difference from the STD ranking does not indicate an inconsistency, because DEL depends on the amplitudes and occurrence of individual rainflow-counted load cycles and is therefore particularly sensitive to intermittent large-amplitude fluctuations. This indicates that partial wake does not necessarily correspond to the lowest mean aerodynamic output, but it can significantly aggravate fatigue damage because of the stronger load unsteadiness. It is also worth noting that, even when the mean inflow condition approaches the free-stream state at larger lateral offsets, residual wake-induced non-uniformity can still maintain the fatigue load above the fully recovered level. Overall, in the design of floating wind farms, sufficient attention should be paid to the increase in blade fatigue loads and the associated potential safety risks under partial wake conditions.

To further examine the differences between FOWTs and FBWTs under partial-wake conditions, an additional FBWT case is performed for the representative configuration with a streamwise spacing of 5*D* and a lateral offset of 1/2*D*. The corresponding time histories of thrust, power, and MOoP of WT1 are compared in Appendix A. Overall, the floating and fixed-bottom configurations exhibit similar temporal variation patterns and comparable response levels. Nevertheless, some differences in the fluctuation amplitudes remain, particularly for thrust and power, indicating that platform motion can modify the unsteady aerodynamic response without fundamentally changing the overall response characteristics under the representative partial-wake condition.

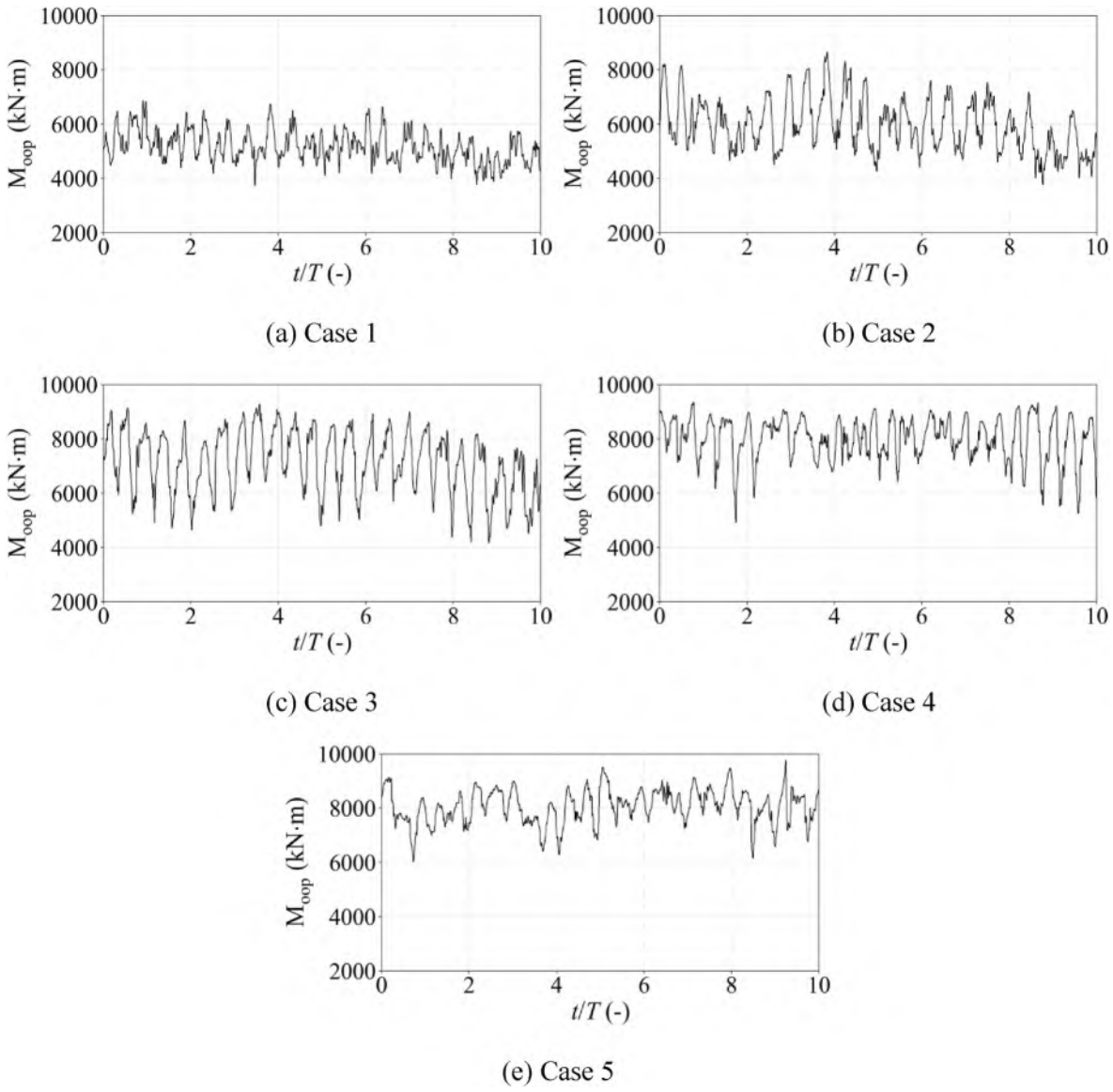

Fig. 19. Time histories of the MOoP of WT1.

Table 4
Statistical results of the MOoP and normalized DEL of WT1.

Cases	Mean (kN·m)	Max (kN·m)	Min (kN·m)	STD (kN·m)	Normalized DEL
1	5218.83	7315.35	3722.46	609.62	1.02
2	6006.10	8649.28	3767.72	972.41	1.37
3	7195.35	9274.23	4167.27	1134.78	1.48
4	8039.79	9356.87	4926.91	775.37	1.29
5	8062.23	9743.34	6017.45	618.51	1.07
6	6017.41	8182.38	4267.88	735.76	1.12
7	6704.19	9097.48	4561.26	822.79	1.29
8	7490.48	9274.08	5009.25	912.51	1.26
9	8051.43	9436.24	5844.06	698.8	1.08
10	8213.18	9417.91	6454.81	546.79	0.85

4.4. Wake characteristics

This section examines the wake characteristics of FOWTs under different partial wake conditions. The data over approximately the last ten wave periods are selected for analysis. Fig. 20 shows the streamwise velocity contours on the horizontal plane at hub height for Cases 1 to 5 with a streamwise spacing of 5*D*. The left column presents the instantaneous streamwise velocity contours, while the right column shows the time-averaged streamwise velocity contours. It should be noted that the horizontal coordinates in Fig. 20 are referenced to the rotor center of WT0. For the vertical plane results shown later, the streamwise coordinate is also referenced to the rotor center of WT0, while the vertical coordinate is referenced to the free surface. Unless otherwise specified, the same definitions are adopted in the following wake analysis. From the instantaneous results, pronounced time-varying flow structures can be observed near the wake shear layer. This indicates that the wake structure exhibits strong unsteadiness under the combined effects of ABL turbulence and platform motion. Meanwhile, clear wake meandering is observed in the wake regions of both the upstream and downstream FOWTs, indicating that the wake center undergoes lateral oscillation and evolution with time. From the time-averaged results, the superposition of the wakes of the upstream and downstream turbines further enhances the velocity deficit in the downstream region of WT1. As the lateral offset increases, the velocity deficit in the wake of WT1 generally becomes weaker. According to the previous analysis, although the inflow condition of Case 4 is already close to the free-stream state, its wake still exhibits evident lateral asymmetry, with a larger velocity

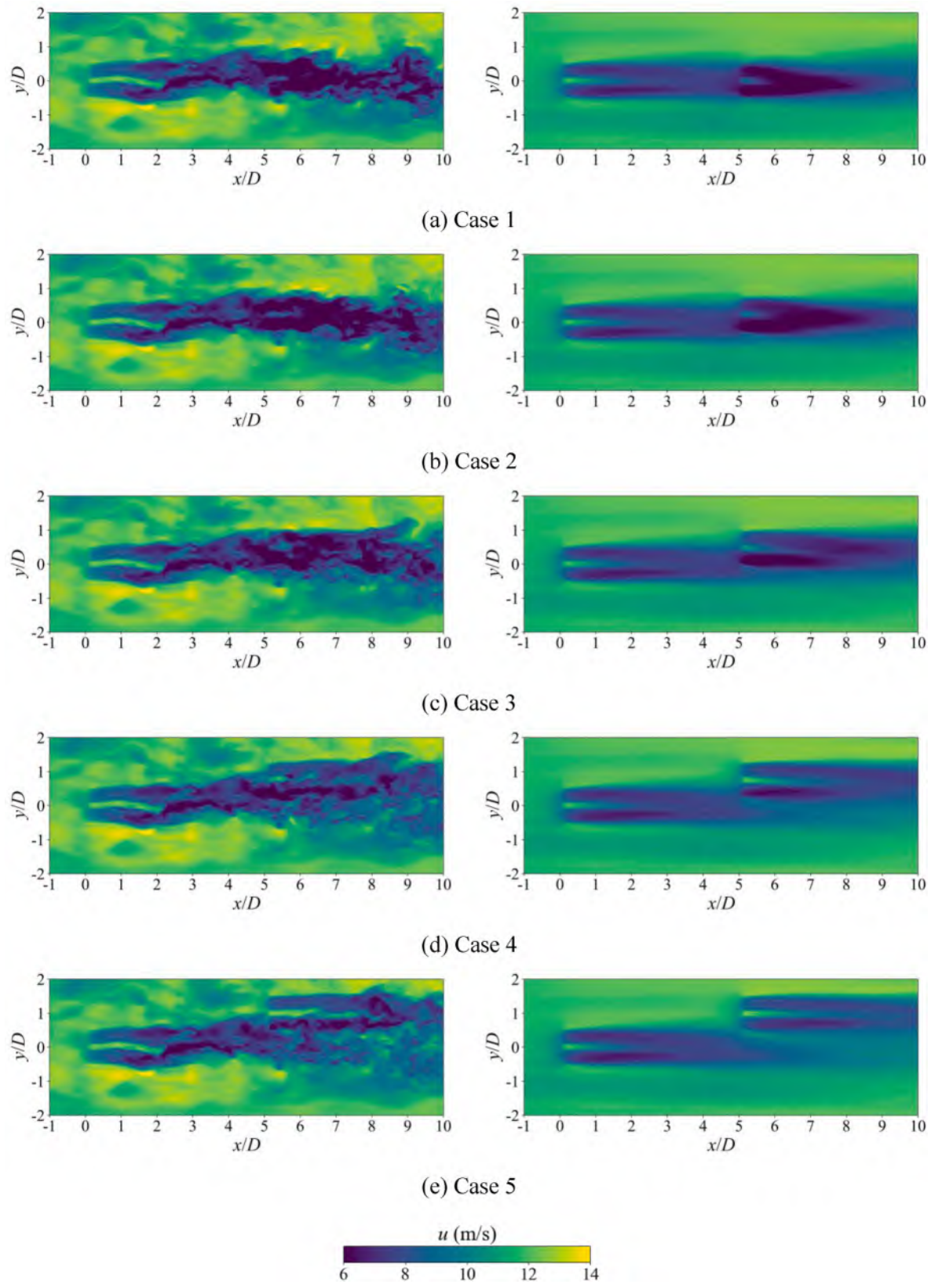

Fig. 20. The streamwise velocity contours on the horizontal plane at hub height.

deficit on the side closer to the wake of WT0 than on the other side. This indicates that the influence of the upstream wake on the rotor disk of WT1 has not been fully eliminated, and the local inflow still remains strongly non-uniform, which is further transmitted into the downstream wake development. By contrast, in Case 5 with a lateral offset of 1*D*, the influence of the upstream turbine on the wake of WT1 is significantly weakened, and the wake characteristics become closer to those of a turbine under free-stream inflow conditions, which is more favorable for

the arrangement of turbines further downstream. The cases with a streamwise spacing of 7*D* exhibit the same overall dependence on lateral offset, although the quantitative wake characteristics differ because of the additional downstream development of the upstream wake.

Fig. 21 presents the time-averaged streamwise velocity contours on the vertical plane through the rotor center of WT0. It can be seen that the time-averaged wake exhibits an upward shift in the vertical direction. This behavior is likely associated with the mean platform pitch and the resulting inclination of the rotor plane relative to the fixed condition, which causes a corresponding displacement of the wake center (Xu et al., 2024). Meanwhile, the results on the vertical plane also more clearly reflect the variation in wake interaction between the upstream and downstream turbines under different cases. As the lateral offset increases, the wake superposition and mixing between WT0 and WT1 on the vertical plane gradually weaken. For the 5*D* cases, in the region downstream of WT1, the additional wake effect induced by WT1 is already significantly weakened in Cases 4 and 5, indicating that the wake interaction between the two turbines has been greatly reduced. Table 5 gives the time- and rotor-averaged streamwise velocity within the projected rotor disk at downstream locations corresponding to WT1 under different cases. The streamwise velocity in the table is normalized using the inflow wind speed of 11.4 m/s. It is worth noting that, with increasing lateral offset, the mean streamwise velocity within the projected rotor disk at fixed downstream positions relative to WT1 does not exhibit a monotonic increasing trend. This indicates that, in terms of wake recovery in the coordinate system relative to WT1, a competition exists between the weakening of the partial wake effect and the enhancement of energy extraction by WT1 itself. Specifically, a larger lateral offset improves the inflow condition of WT1 and weakens the wake interference from WT0. At the same time, however, the higher inflow velocity also enhances the aerodynamic loading and energy extraction of WT1, thereby generating a more pronounced velocity deficit in its own wake. Therefore, at fixed downstream distances relative to WT1, the mean streamwise velocity does not necessarily increase monotonically with lateral offset. The 7*D* cases exhibit the same qualitative behavior, and the downstream velocity of WT1 is not necessarily higher than that of the corresponding 5*D* case despite the improved inflow condition, because the increased energy extraction of WT1 also strengthens its own wake deficit. By contrast, if the local mean wind speed is examined at a fixed absolute position in the wind farm, the superposed wake effect of the two turbines at that location is usually weakened as the lateral offset increases, and a higher mean wind speed is therefore obtained.

Table 5
Time- and rotor-averaged normalized streamwise velocity within the projected rotor disk downstream of WT1.

Cases	$x/D = 3$	$x/D = 4$	$x/D = 5$
1	69.12%	74.97%	78.61%
2	69.78%	75.04%	78.56%
3	69.53%	73.42%	76.42%
4	70.50%	73.25%	75.38%
5	73.26%	75.91%	77.94%
6	69.19%	73.64%	77.72%
7	70.50%	74.66%	78.79%
8	69.97%	73.72%	76.83%
9	70.61%	73.20%	75.44%
10	72.40%	75.17%	76.77%

Fig. 22 presents the streamwise velocity deficit profiles on the horizontal plane at hub height and on the vertical plane through the rotor center of WT0. For WT0 under free-stream inflow conditions, the velocity deficit profile on the horizontal plane exhibits a distinct double-peak distribution in the near-wake region and gradually transitions to

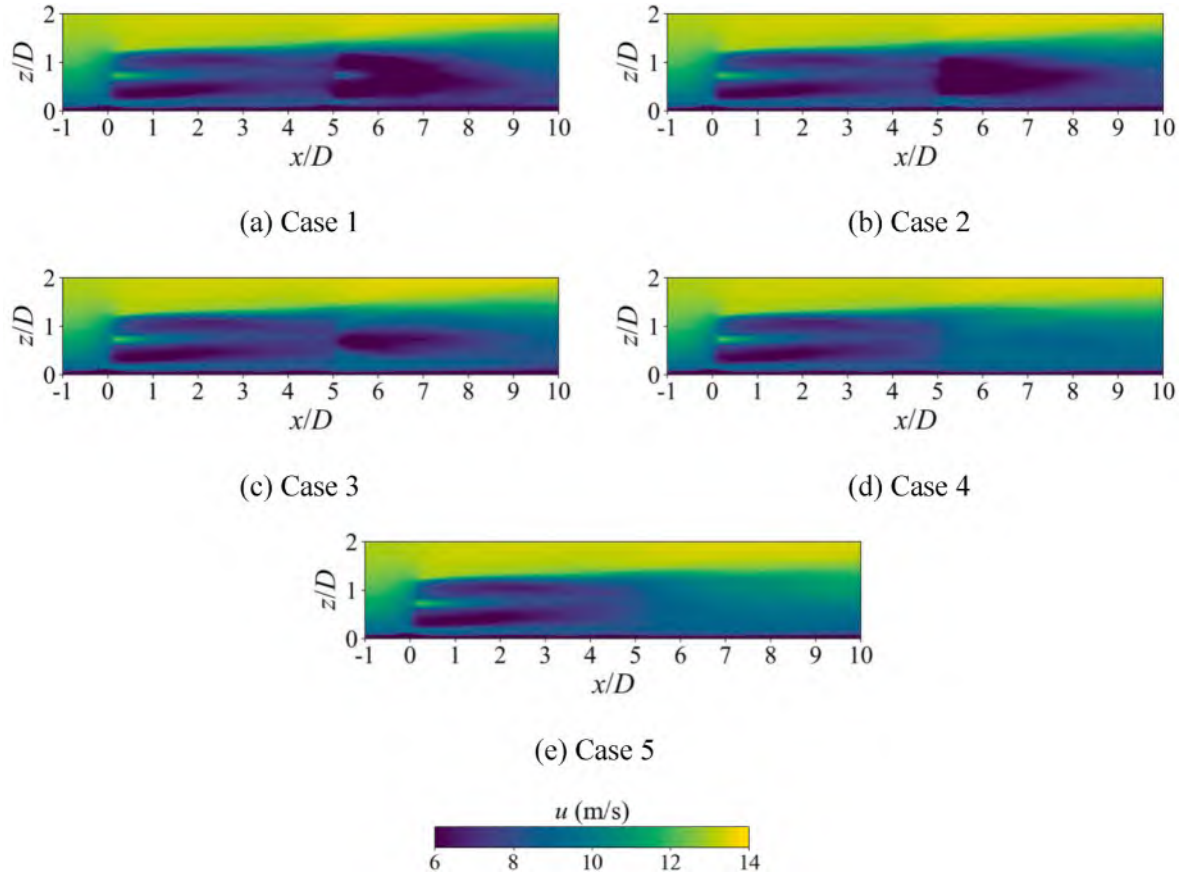

Fig. 21. The time-averaged streamwise velocity contours on the vertical plane through the rotor center.

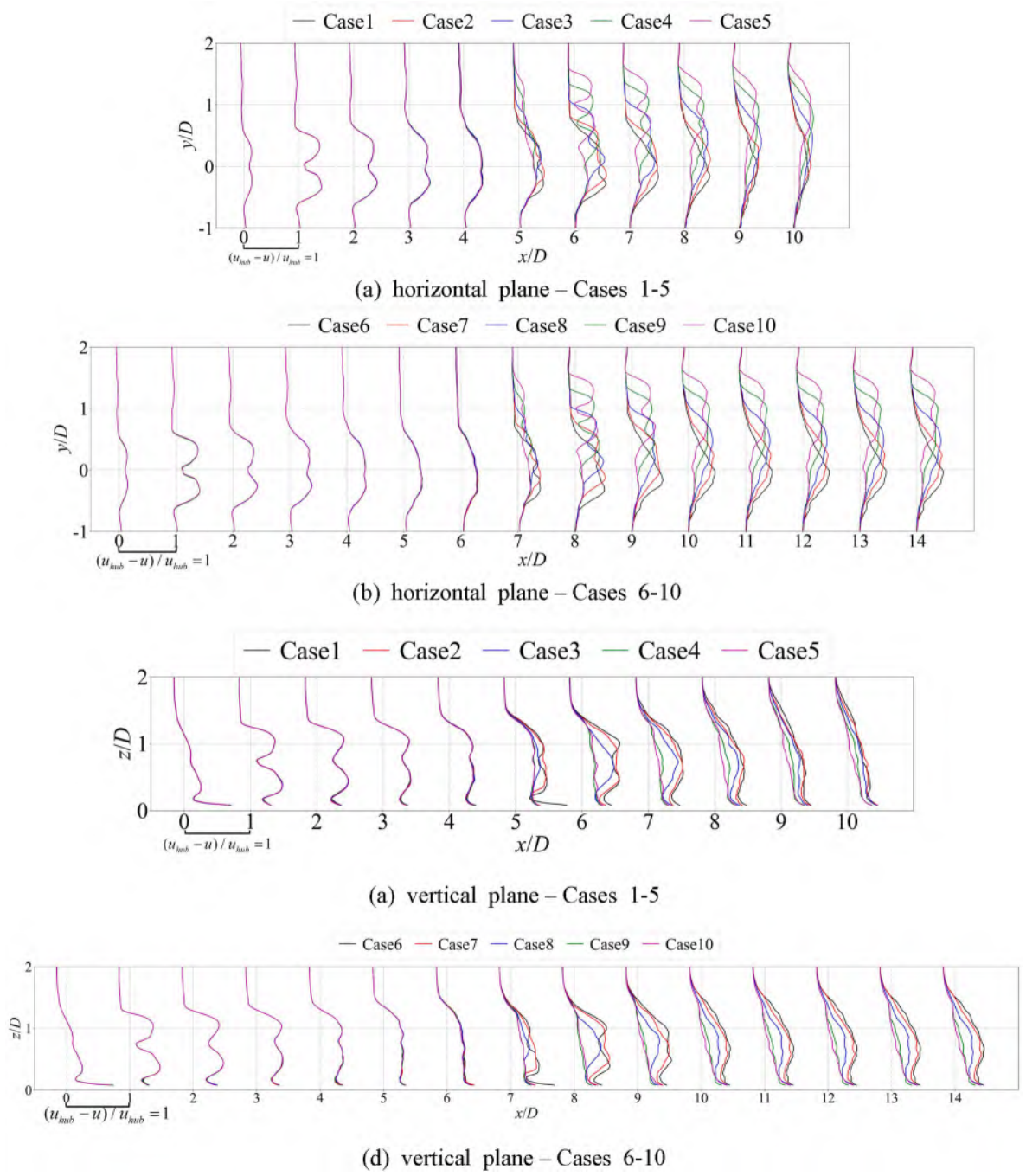

Fig. 22. The streamwise velocity deficit profiles on the horizontal plane at hub height and the vertical plane through the WT0 rotor center.

a single-peak distribution during downstream development. By contrast, for WT1 under different partial wake conditions, the wake deficit profiles in Cases 1, 2, and 3 have already evolved into a single-peak distribution at 2*D* downstream. The corresponding 7*D* cases show similar profile evolution, indicating that this feature is primarily associated with the disturbed inflow of WT1 rather than with a specific streamwise spacing. This is attributed partly to the stronger turbulent and wake-disturbed inflow conditions encountered by WT1, which enhance wake mixing. On the other hand, partial wake causes the inflow over the rotor disk of WT1 to become strongly non-uniform, thereby modifying the initial structure of its near wake and leading to wake evolution characteristics different from those of a single turbine under free-stream inflow. The horizontal profiles further show that, within 3*D* downstream of WT1, the peak velocity deficits are generally larger under small lateral-offset conditions than under larger offsets. This is mainly because, under small lateral offset conditions, WT1 is still strongly affected by the upstream wake, and the low-velocity regions of the upstream and downstream turbine wakes continue to overlap downstream, resulting in a deeper local velocity deficit. As the downstream distance further increases, the peak velocity deficits among the different cases gradually become closer. This indicates that, with enhanced wake mixing, the additional wake effect from WT0 is gradually weakened. At the same time, under larger lateral offset conditions, the stronger energy extraction by WT1 itself also begins to play a more evident role in wake deficit formation, thereby partially offsetting the differences among the cases. The vertical profiles show that, as the lateral offset increases, the influence of the wake of WT1 on the vertical plane passing through the rotor center of WT0 is significantly reduced. However, even at 10*D*

downstream, an evident velocity deficit is still observed, indicating that the overall wake effect of the two-turbine system can persist over a long downstream distance, although the additional influence of WT1 on the wake structure within this vertical plane gradually weakens as the lateral offset increases. Fig. 23 presents the turbulence intensity profiles on the horizontal plane at hub height. Overall, the turbulence intensity profiles under all cases exhibit a double-peak distribution, with the peaks mainly located near the wake shear layers. The peak turbulence intensities downstream of WT1 are generally higher under small lateral-offset conditions, which is consistent with the stronger wake superposition and more intense shear indicated by the velocity deficit results. In addition, as the lateral offset varies, the locations of both the peak velocity deficit and the peak turbulence intensity also shift noticeably, reflecting adjustments in the wake center position and shear-layer structure of WT1 under different partial wake conditions.

Fig. 24 shows the vortex structures of the FOWTs. The vortical structures are identified using the Q criterion and are colored by the streamwise velocity. It can be seen that relatively clear ring-shaped blade-tip vortices are observed in the near-wake region of WT0, but these vortex structures break down rapidly as the downstream distance increases. This is mainly because, under ABL inflow conditions, turbulent vortical structures are already present in the free-stream region, and their interaction with the turbine-generated vortices promotes earlier breakdown of the blade-tip vortices (Xu et al., 2024). For WT1, the vortex ring structures are closely related to the lateral offset. In Cases 1 and 2, since WT1 is still subjected to strong wake interference from the upstream turbine, the ring-shaped vortex structures behind it become difficult to distinguish, indicating that the blade-tip vortices undergo significant breakdown and mixing at a relatively short downstream distance. As the lateral offset increases to approximately 1/2*D*, identifiable vortex-ring structures begin to appear behind WT1. At larger lateral offsets of 3/4*D* and 1*D*, these structures become more continuous and clearer. The 7*D* cases exhibit the same overall evolution with lateral offset, with discernible vortex-ring structures also appearing around the 1/2*D* offset and becoming progressively clearer at larger offsets. This is likely because, under small lateral offset conditions, the inflow of WT1 exhibits stronger non-uniformity and a higher turbulence level, which weakens the coherence of the vortical structures in the near-wake region and leads to earlier breakdown of the blade-tip vortices. By contrast, under large lateral offset conditions, the inflow of WT1 gradually recovers, allowing the blade-tip vortices to maintain a more complete evolution process. This result is consistent with the previous analyses of aerodynamic and wake characteristics, namely that stronger wake superposition not only leads to larger local velocity deficits and turbulence intensities, but is also associated with more complex wake vortex structures.

Overall, partial wake not only alters the inflow conditions and aerodynamic responses of WT1, but also significantly affects the velocity deficit profiles, recovery process, turbulence distribution, and vortex structure evolution in its downstream wake. Under small lateral-offset conditions, WT1 remains strongly affected by the upstream wake, and its downstream wake exhibits a deeper velocity deficit, higher turbulence intensity, and earlier vortex breakdown, indicating stronger wake interaction between the two turbines. As the lateral offset increases, the inflow conditions of WT1 are gradually improved, and its wake structure and evolution progressively recover toward those of a single turbine under free-stream inflow conditions. At intermediate lateral offsets, although the mean inflow of WT1 may already recover substantially, residual wake asymmetry and inflow non-uniformity can still affect its downstream wake development. The results obtained for the 5*D* and 7*D* streamwise spacings show a consistent qualitative dependence on lateral offset, although quantitative differences remain in the inflow,

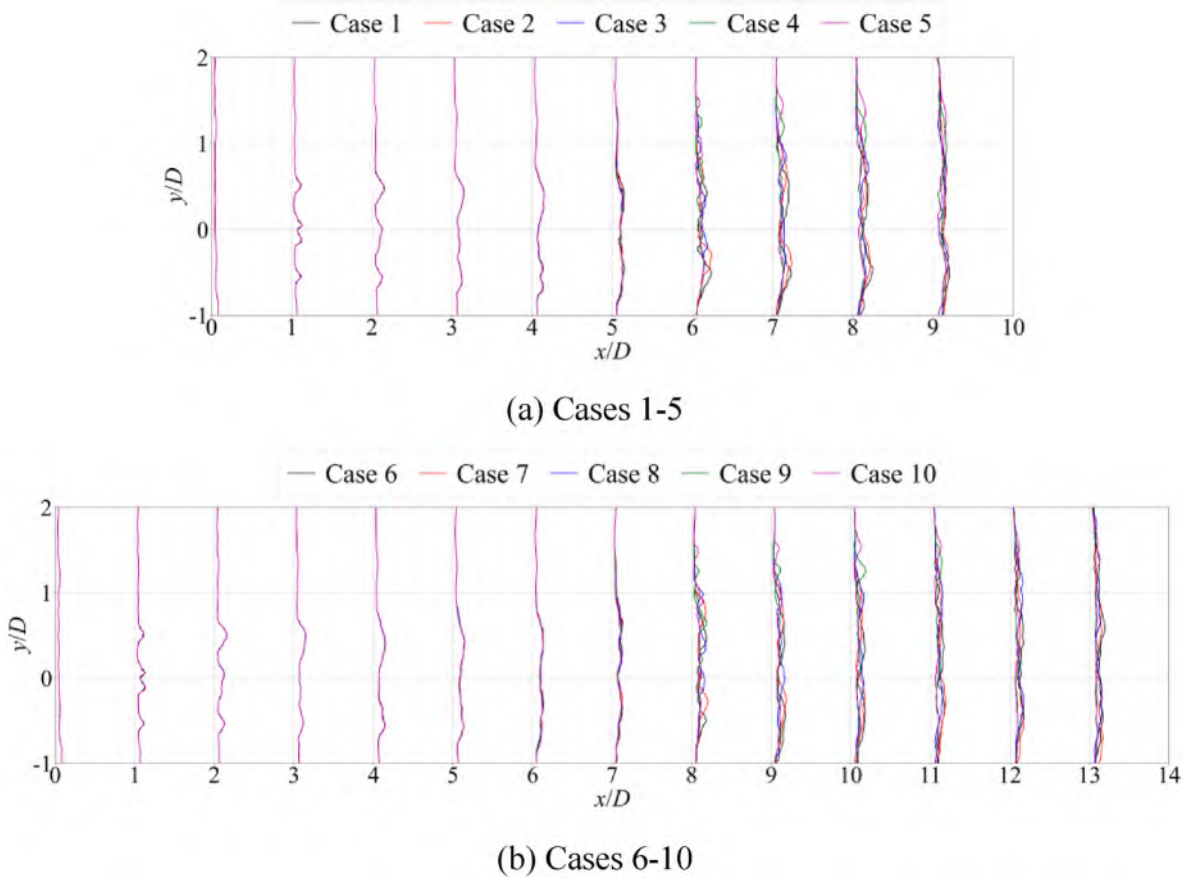

Fig. 23. The turbulence intensity profiles on the horizontal plane at hub height.

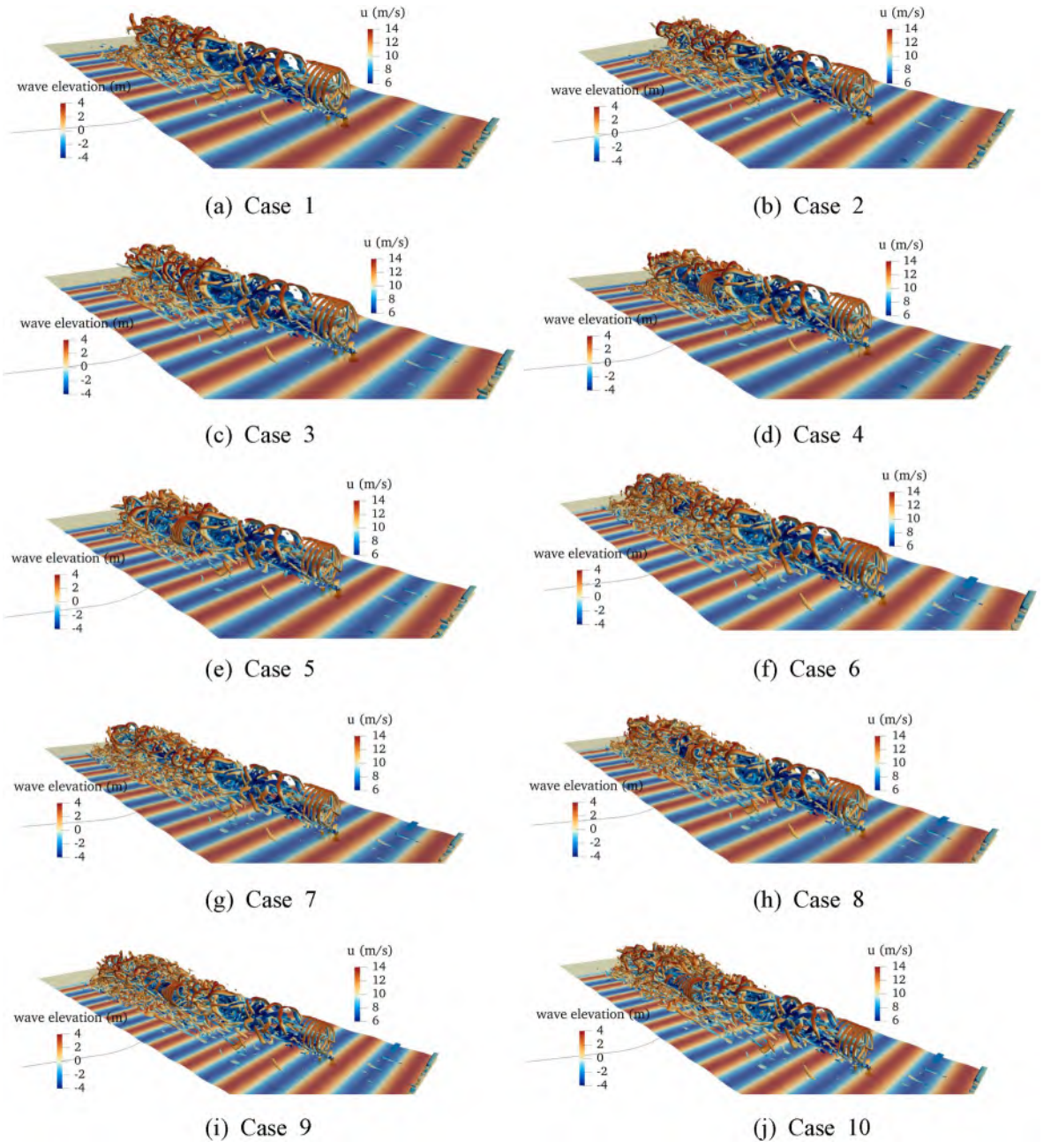

Fig. 24. Vortical structures of the FOWTs.

aerodynamic response, and downstream wake characteristics. For both streamwise spacings considered here, when the lateral offset increases to 1*D*, the direct influence of WT0 on WT1 and its downstream wake structure is significantly weakened. This suggests that a sufficiently large lateral offset can help alleviate direct wake interference, although the optimal layout of further downstream turbines still needs to be evaluated by considering additional factors such as farm-scale interactions and environmental conditions.

5. Conclusion

In this study, the FOWT-UALM-SJTU solver is used to conduct fully coupled simulations of two FOWTs under different partial wake conditions. Two streamwise spacings of 5*D* and 7*D* are considered, while the lateral offset of the downstream turbine WT1 is varied from 0*D* to 1*D*. The inflow, platform motion, aerodynamic response, and wake characteristics of WT1 are analyzed in detail. The main conclusions are summarized as follows:

(1) The inflow conditions of WT1 are strongly affected by the lateral offset. As the lateral offset increases from 0*D* to 1*D*, the rotor-averaged inflow velocity generally increases, whereas the inflow non-uniformity varies non-monotonically and becomes most pronounced at intermediate lateral offsets. For both the 5*D* and 7*D* spacings, the largest spatial standard deviation is observed near the 1/2*D* partial wake condition, while the overall inflow non-uniformity is lower at the 7*D* spacing because of the additional wake recovery before reaching WT1. The platform motion results show that the mean surge and pitch responses generally increase with increasing lateral offset, whereas their fluctuation intensities differ only slightly among the cases. This indicates that the influence of partial wake on platform motion is

mainly reflected in the mean response level rather than in the fluctuation intensity.

(2) The mean aerodynamic performance and unsteady aerodynamic response of WT1 exhibit different trends. As the lateral offset increases, the mean thrust and power of WT1 increase gradually. However, their fluctuation intensities become most pronounced under partial wake conditions, with the strongest fluctuations observed at the 1/2*D* lateral offset, followed by the 1/4*D* lateral offset, for both streamwise spacings. Although the corresponding fluctuation levels at the 7*D* spacing are generally lower than those at 5*D*, their dependence on lateral offset remains consistent. This indicates that the fully waked condition does not necessarily correspond to the strongest unsteady aerodynamic response. Instead, when the rotor is located in the transition region between the wake core and the free-stream region, stronger inflow non-uniformity and wake meandering induce more severe thrust and power fluctuations.

(3) Partial wake significantly enhances blade-load unsteadiness and increases fatigue risk. The AOA and MOoP results show stronger unsteady responses under intermediate partial wake conditions, consistent with the enhanced inflow non-uniformity. For the 5*D* spacing, the 1/2*D* partial wake case exhibits the largest normalized DEL, approximately 45% higher than that of the corresponding fully waked case. The 7*D* cases show a similar overall variation in fatigue loading with lateral offset. This suggests that partial wake does not necessarily correspond to the lowest mean aerodynamic output, but can significantly increase fatigue damage risk because of stronger load unsteadiness. It is worth noting that, although the mean inflow of WT1 at the 3/4*D* lateral offset is already close to the free-stream condition for both streamwise spacings, the DEL still remains at a relatively high level, indicating that the influence of residual wake asymmetry on fatigue loading cannot be neglected.

(4) The wake evolution of WT1 also strongly depends on the lateral offset. Under small lateral offset conditions, WT1 is still subjected to strong upstream wake interference, and its downstream wake exhibits a deeper local velocity deficit, higher turbulence-intensity peaks, and earlier breakdown of blade-tip vortices. As the lateral offset increases, the wake structure and recovery of WT1 progressively approach those of a single turbine under free-stream inflow. The two streamwise spacings exhibit the same overall dependence on lateral offset, although quantitative differences are observed in the downstream wake characteristics. In particular, when the lateral offset reaches 1*D*, the direct influence of WT0 on WT1 and its downstream wake is significantly weakened. These results suggest that a sufficiently large lateral offset can help alleviate direct wake interference.

This study provides insights into the design and wake analysis of floating wind farms under different layout configurations. Future work should extend the present analysis to multi-turbine layouts under different inflow and wave conditions, further investigate the differences between FOWTs and FBWTs under comparable wake configurations, and develop engineering wake models applicable to floating wind farms.

CRediT authorship contribution statement

Mingqiu Liu: Writing – original draft, Visualization, Validation, Software, Methodology, Investigation, Formal analysis, Data curation, Conceptualization. **Yao Zhong:** Writing – review & editing, Validation, Resources, Investigation, Data curation. **Weiwen Zhao:** Writing – review & editing, Validation, Supervision, Software, Resources, Project administration, Formal analysis, Conceptualization. **Decheng Wan:** Writing – review & editing, Supervision, Methodology, Funding acquisition, Conceptualization.

Declaration of competing interest

The authors declare that they have no known competing financial interests or personal relationships that could have appeared to influence the work reported in this paper.

Acknowledgments

This work is supported by the National Key Research and Development Program of China (Grant No. 2025YFF0519800), and National Natural Science Foundation of China (No. 52131102), to which the authors are most grateful.

Appendix A

To provide a further comparison between FOWTs and FBWTs under partial-wake conditions, the configuration with a streamwise spacing of 5*D* and a lateral offset of 1/2*D* is selected as a representative case. As discussed above, this configuration is characterized by pronounced inflow non-uniformity over the downstream rotor and correspondingly strong unsteady aerodynamic responses. A fixed-bottom case with the same turbine arrangement and atmospheric boundary layer inflow is therefore considered for comparison, with the analysis focusing on the aerodynamic responses of the downstream turbine WT1.

Fig. 25 compares the time histories of power, thrust, and MOoP of WT1 for the floating and fixed-bottom configurations. In general, the two configurations exhibit similar temporal variation patterns and comparable response levels. Previous studies have also reported relatively small differences in aerodynamic responses and wake characteristics between FOWTs and FBWTs under ABL inflow, while atmospheric turbulence plays a dominant role in the aerodynamic fluctuations (Xu et al., 2023). In the present partial-wake condition, the strongly non-uniform wake inflow plays an important role in the overall response of the downstream turbine. Nevertheless, differences are still observed in the detailed temporal fluctuations of thrust and power, while MOoP shows a broadly similar response between the two configurations. These results suggest that, for the representative configuration, the FOWT and FBWT exhibit broadly similar overall aerodynamic response characteristics under partial-wake inflow, while some differences remain in the detailed unsteady responses.

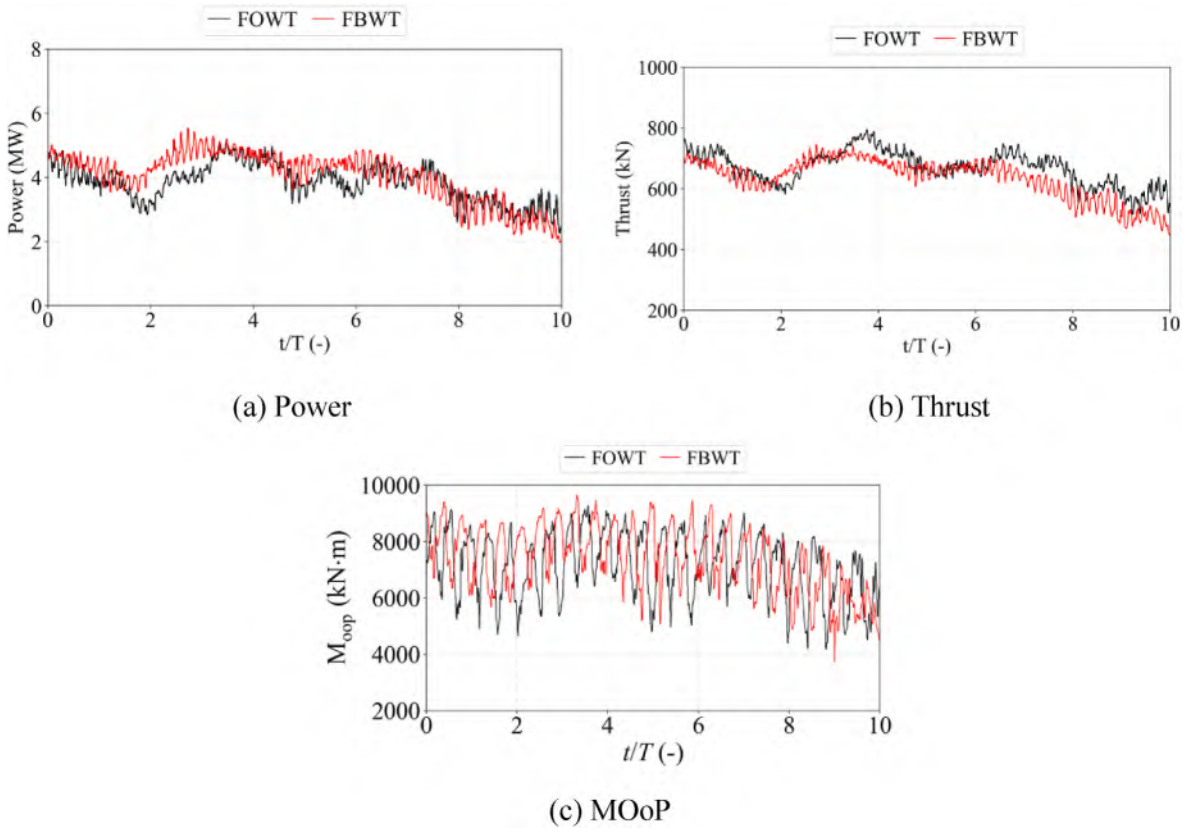

Fig. 25. The time histories of thrust, power, and MOoP of WT1 for the FOWT and FBWT.

References

Arabgolarcheh, A., Micallef, D., Benini, E., 2023a. The impact of platform motion phase differences on the power and load performance of tandem floating offshore wind turbines. Energy 284, 129271. https://doi.org/10.1016/j.energy.2023.129271.

Arabgolarcheh, A., Micallef, D., Rezaeiha, A., Benini, E., 2023b. Modelling of two tandem floating offshore wind turbines using an actuator line model. Renew. Energy 216, 119067. https://doi.org/10.1016/j.renene.2023.119067.

Bhattacharya, S., Nikitas, G., 2025. Wind energy: status and outlook with focus on offshore wind. In: Energy and Climate Change. Elsevier, pp. 197–224. https://doi.org/10.1016/B978-0-443-21927-6.00014-3.

Cai, Y., Zhao, H., Li, X., Liu, Y., 2023. Aerodynamic analysis for different operating states of floating offshore wind turbine induced by pitching movement. Energy 285, 129538. https://doi.org/10.1016/j.energy.2023.129538.

Campaña-Alonso, G., Ferrer, E., Méndez-López, B., 2024. Wind turbine power extraction under partial wake operations, a CFD study using ALM. J. Phys., Conf. Ser. 2767, 092097. https://doi.org/10.1088/1742-6596/2767/9/092097.

Cao, H., Wang, X., Liu, Y., Wan, D., 2013. Numerical prediction of wave loading on a floating platform coupled with a mooring system. Presented at the twenty-third International Offshore and Polar Engineering Conference. ISOPE-I-13-325.

Cao, H.-J., Wan, D.-C., 2014. Development of multidirectional nonlinear numerical wave tank by Naoe-FOAM-SJTU solver. International Journal of Ocean System Engineering 4, 49–56. https://doi.org/10.5574/IJOSE.2014.4.1.049.

Chen, Z., Wang, X., Guo, Y., Kang, S., 2021. Numerical analysis of unsteady aerodynamic performance of floating offshore wind turbine under platform surge and pitch motions. Renew. Energy 163, 1849–1870. https://doi.org/10.1016/j.renene.2020.10.096.

Cheng, P., Huang, Y., Wan, D., 2019. A numerical model for fully coupled aero-hydrodynamic analysis of floating offshore wind turbine. Ocean. Eng. 173, 183–196. https://doi.org/10.1016/j.oceaneng.2018.12.021.

Churchfield, M.J., Lee, S., Michalakes, J., Moriarty, P.J., 2012. A numerical study of the effects of atmospheric and wake turbulence on wind turbine dynamics. J. Turbul. 13, N14. https://doi.org/10.1080/14685248.2012.668191.

Fang, Y., Li, G., Duan, L., Han, Z., Zhao, Y., 2021. Effect of surge motion on rotor aerodynamics and wake characteristics of a floating horizontal-axis wind turbine. Energy 218, 119519. https://doi.org/10.1016/j.energy.2020.119519.

Fleming, P., Gebraad, P.M.O., Lee, S., Van Wingerden, J.-W., Johnson, K., Churchfield, M., Michalakes, J., Spalart, P., Moriarty, P., 2015. Simulation comparison of wake mitigation control strategies for a two-turbine case. Wind Energy 18, 2135–2143. https://doi.org/10.1002/we.1810.

Gao, X., Zhou, K., Liu, R., Ma, W., Gong, X., Zhu, X., Wang, Y., Zhao, F., 2024. Aerodynamic characteristics of wind turbines considering the inhomogeneity and periodic incentive of wake effects. Energy 310, 133275. https://doi.org/10.1016/j.energy.2024.133275.

Guo, Y., Wang, X., Mei, Y., Ye, Z., Guo, X., 2022. Effect of coupled platform pitch-surge motions on the aerodynamic characters of a horizontal floating offshore wind turbine. Renew. Energy 196, 278–297. https://doi.org/10.1016/j.renene.2022.06.108.

Huang, Y., Wan, D., 2019. Investigation of interference effects between wind turbine and spar-type floating platform under combined wind-wave excitation. Sustainability 12, 246. https://doi.org/10.3390/su12010246.

Huang, Y., Zhao, W., Wan, D., 2023. Wake interaction between two spar-type floating offshore wind turbines under different layouts. Phys. Fluids 35, 097102. https://doi.org/10.1063/5.0161759.

Jonkman, J., Butterfield, S., Musial, W., Scott, G., 2009. Definition of a 5-MW reference wind turbine for offshore system development. No. NREL/TP-500-38060, 947422. https://doi.org/10.2172/947422.

Kang, Y., Lee, S., 2024. Wake effect on floating offshore wind turbine fatigue load. Phys. Fluids 36, 125176. https://doi.org/10.1063/5.0242835.

Li, L., Liu, Y., Yuan, Z., Gao, Y., 2018. Wind field effect on the power generation and aerodynamic performance of offshore floating wind turbines. Energy 157, 379–390. https://doi.org/10.1016/j.energy.2018.05.183.

Li, X., Xiao, Q., Huang, Y., 2025. The impact of platform motion on the aerodynamic characteristics of floating offshore wind turbine arrays. Phys. Fluids 37, 037102. https://doi.org/10.1063/5.0256441.

Li, X., Xiao, Q., Wang, E., Peyrard, C., Gonçalves, R.T., 2023. The dynamic response of floating offshore wind turbine platform in wave–current condition. Phys. Fluids 35, 087113. https://doi.org/10.1063/5.0158917.

Li, Y., Yu, W., Sarlak, H., 2024. Wake structures and performance of wind turbine rotor with harmonic surging motions under laminar and turbulent inflows. Wind Energy 27, 1499–1525. https://doi.org/10.1002/we.2949.

Li, Z., Dong, G., Yang, X., 2022. Onset of wake meandering for a floating offshore wind turbine under side-to-side motion. J. Fluid Mech. 934, A29. https://doi.org/10.1017/jfm.2021.1147.

Lin, M., Porté-Agel, F., 2022. Large-eddy simulation of a wind-turbine array subjected to active yaw control. Wind Energ. Sci. 7, 2215–2230. https://doi.org/10.5194/wes-7-2215-2022.

Liu, M., Zhong, Y., Zhao, W., Wan, D., 2025. Effect of coupled surge–pitch motions on the wake characteristics of floating offshore wind turbines under atmospheric boundary layer inflows. Phys. Fluids 37, 115115. https://doi.org/10.1063/5.0293258.

Liu, Y., Xiao, Q., Incecik, A., Peyrard, C., Wan, D., 2017. Establishing a fully coupled CFD analysis tool for floating offshore wind turbines. Renew. Energy 112, 280–301. https://doi.org/10.1016/j.renene.2017.04.052.

Moeng, C.-H., 1984. A large-eddy-simulation model for the study of planetary boundary-layer turbulence. J. Atmos. Sci. 41, 2052–2062. https://doi.org/10.1175/1520-0469(1984)041%3C2052:ALESMF%3E2.0.CO;2.

Ning, X., Wan, D., 2019. LES study of wake meandering in different atmospheric stabilities and its effects on wind turbine aerodynamics. Sustainability 11, 6939. https://doi.org/10.3390/su11246939.

Porté-Agel, F., Bastankhah, M., Shamsoddin, S., 2020. Wind-turbine and wind-farm flows: a review. Boundary-Layer Meteorol. 174, 1–59. https://doi.org/10.1007/s10546-019-00473-0.

Rezaeiha, A., Micallef, D., 2021. Wake interactions of two tandem floating offshore wind turbines: CFD analysis using actuator disc model. Renew. Energy 179, 859–876. https://doi.org/10.1016/j.renene.2021.07.087.

Robertson, A., Jonkman, J., Masciola, M., Song, H., Goupee, A., Coulling, A., Luan, C., 2014. Definition of the Semisubmersible Floating System for Phase II of OC4. https://doi.org/10.2172/1155123. No. NREL/TP-5000-60601, 1155123).

Sant, T., 2026. Progress in the modelling and management of offshore wind farm wakes: a literature review. Ocean. Eng. 352, 124544. https://doi.org/10.1016/j.oceaneng.2026.124544.

Shen, Z., Wan, D., 2014. RANS computations of added resistance and motions of a ship in head waves. Int. J. Offshore Polar Eng. 23, 264–271.

Sørensen, J.N., Shen, W.Z., 2002. Numerical modeling of wind turbine wakes. J. Fluid Eng. 124, 393–399. https://doi.org/10.1115/1.1471361.

Tran, T.T., Kim, D.-H., 2016. A CFD study into the influence of unsteady aerodynamic interference on wind turbine surge motion. Renew. Energy 90, 204–228. https://doi.org/10.1016/j.renene.2015.12.013.

Troldborg, N., Sørensen, J.N., Mikkelsen, R., 2007. Actuator line simulation of wake of wind turbine operating in turbulent inflow. J. Phys., Conf. Ser. 75, 012063. https://doi.org/10.1088/1742-6596/75/1/012063.

Wang, J., Zhao, W., Wan, D., 2019. Development of naoe-FOAM-SJTU solver based on OpenFOAM for marine hydrodynamics. J. Hydrodyn. 31, 1–20. https://doi.org/10.1007/s42241-019-0020-6.

Wang, K., Chen, S., Chen, J., Zhao, M., Lin, Y., 2024. Study on wake characteristics of fixed wind turbines and floating wind turbines arranged in tandem. Ocean. Eng. 304, 117808. https://doi.org/10.1016/j.oceaneng.2024.117808.

Wang, L., Dong, M., Yang, J., Wang, Lei, Chen, S., Duić, N., Joo, Y.H., Song, D., 2024. Wind turbine wakes modeling and applications: past, present, and future. Ocean. Eng. 309, 118508. https://doi.org/10.1016/j.oceaneng.2024.118508.

Wise, A.S., Bachynski, E.E., 2020. Wake meandering effects on floating wind turbines. Wind Energy 23, 1266–1285. https://doi.org/10.1002/we.2485.

Xu, S., Yang, X., Zhao, W., Wan, D., 2024. Numerical analysis of aero-hydrodynamic wake flows of a floating offshore wind turbine subjected to atmospheric turbulence inflows. Ocean. Eng. 300, 117498. https://doi.org/10.1016/j.oceaneng.2024.117498.

Xu, S., Zhuang, T., Zhao, W., Wan, D., 2023. Numerical investigation of aerodynamic responses and wake characteristics of a floating offshore wind turbine under atmospheric boundary layer inflows. Ocean. Eng. 279, 114527. https://doi.org/10.1016/j.oceaneng.2023.114527.

Xu, X., Shen, X., Wang, S., Xing, Y., Yang, P., Ye, Y., Ji, R., Xu, L., 2025. Effects of wake-added turbulence on extreme loads and fatigue damage of floating offshore wind turbines. Phys. Fluids 37, 105138. https://doi.org/10.1063/5.0294356.

Xue, L., Wang, J., Zhao, L., Wei, Z., Yu, M., Xue, Y., 2022. Wake interactions of two tandem semisubmersible floating offshore wind turbines based on FAST. Farm. JMSE 10, 1962. https://doi.org/10.3390/jmse10121962.

Yang, H., Ge, M., Gu, B., Du, B., Liu, Y., 2022. The effect of swell on marine atmospheric boundary layer and the operation of an offshore wind turbine. Energy 244, 123200. https://doi.org/10.1016/j.energy.2022.123200.

Yu, Z., Ma, Q., Zheng, X., Liao, K., Sun, H., Khayyer, A., 2023. A hybrid numerical model for simulating aero-elastic-hydro-mooring-wake dynamic responses of floating offshore wind turbine. Ocean. Eng. 268, 113050. https://doi.org/10.1016/j.oceaneng.2022.113050.

Zhang, Y., Kim, B., 2018. A fully coupled computational fluid dynamics method for analysis of semi-submersible floating offshore wind turbines under wind-wave excitation conditions based on OC5 data. Appl. Sci. 8, 2314. https://doi.org/10.3390/app8112314.

Zhao, W., Wan, D., 2015. Numerical study of interactions between phase II of OC4 wind turbine and its semi-submersible floating support system. J. Ocean Wind Energy 2, 45–53.

Zhou, T., Lan, H., Xu, C., Han, X., Wu, X., 2025. Wake and performance of floating offshore wind turbines under six degrees of freedom conditions. Phys. Fluids 37, 015167. https://doi.org/10.1063/5.0246831.

Zhou, Y., Xiao, Q., Liu, Y., Incecik, A., Peyrard, C., Wan, D., Pan, G., Li, S., 2022. Exploring inflow wind condition on floating offshore wind turbine aerodynamic characterisation and platform motion prediction using blade resolved CFD simulation. Renew. Energy 182, 1060–1079. https://doi.org/10.1016/j.renene.2021.11.010.